Research Article

Robust and Recyclable Single-Atom and Cluster-like Cu-Based Catalysts for Methanol Oxidative Carbonylation to Dimethyl Carbonate

Wenjie Li, Shanlin Gao,* Chunbo Lai, Xinling Li, Wanjing Xiao, Xinyu Wang, Huibo Lin, Yang Zhang, Haijun Liu, Gan Yang, Chenghua Xu, Luke J. R. Higgins, Andrew M. Beale, Marc Pera-Titus,* and Zhiyong Deng*

ACCESS | 📊 Metrics & More | 📖 Article Recommendations | 🗄 Supporting Information

ABSTRACT: Methanol oxidative carbonylation is a highly desired reaction for the industrial production of dimethyl carbonate (DMC), offering a more sustainable alternative to the conventional, environmentally unfriendly phosgene-methanol process. Although supported copper nanoparticle catalysts can facilitate this reaction, their rapid deactivation due to Cu sintering and overoxidation limits their industrial applicability. In this study, we present robust and reusable single-atoms and cluster-like Cu catalysts (catalyst loading up to 6.5 wt %) supported on N-doped carbon, synthesized via pyrolysis of Cu-doped ZIF-8 precursors. The formation and stability of highly dispersed Cu species during the reaction was confirmed using a comprehensive suite of characterization techniques, including X-ray diffraction (XRD), Fourier transform infrared (FT-IR), high-resolution transmission electron microscopy (HR-TEM), aberration corrected high angle annular dark field-scanning transmission electron microscopy (AC-HAADF-STEM), X-ray photoelectron spectroscopy (XPS), NH_3-TPD, H_2-TPR, and X-ray absorption spectroscopy (XAS). This unique copper architecture achieved an exceptional DMC selectivity of 99.4% and a space-time yield of 3249 mg $DMC \cdot g^{-1} \cdot h^{-1}$ ($TOF_{DMC,B} = 34.4 \ h^{-1}$; $TOF_{DMC,S} = 294 \ h^{-1}$) at 120 °C for 2 h. The catalysts demonstrated excellent reusability, maintaining their performance over at least seven consecutive runs without deactivation. Postreaction analysis of the spent catalyst after seven runs revealed that Cu was largely free of leaching, sintering, and overoxidation.

KEYWORDS: dimethyl carbonate, ZIF-8, oxidative carbonylation, copper, single atom catalyst
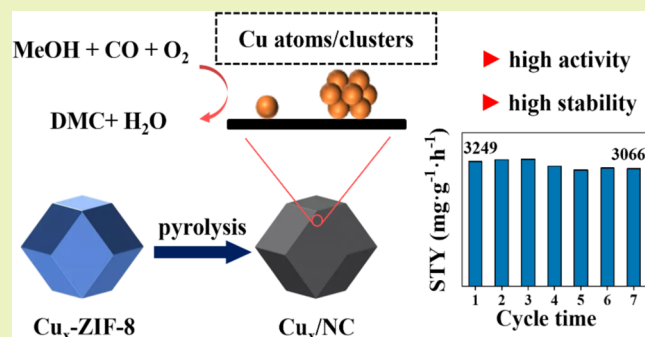
1. INTRODUCTION

Dimethyl carbonate (DMC) is a valuable commodity chemical widely used as a fuel additive, solvent, electrolyte for lithium-ion batteries, and organic building block.[1−3] Traditionally, DMC is synthesized via the reaction of phosgene with methanol, with chloroformate as the primary intermediate. However, due to the toxicity of phosgene, alternative and more sustainable industrial routes have been developed,[3−6] with recent intense R&I efforts notably driven by the Chinese chemical industry. Among these alternatives, the trans-esterification of ethylene (or propylene) carbonate with methanol is a well-established process, offering high DMC yields. Nevertheless, this route is hampered by the high cost of feedstocks—ethylene oxide or propylene oxide—and the generation of excess byproducts, such as ethylene glycol and propylene glycol.[4]

The direct synthesis of DMC from CO_2 and methanol is the greenest route to access DMC, but it is limited by thermodynamics ($\Delta G_{298K} = +25.3 \ kJ \cdot mol^{-1}$), resulting in low conversion that further decreases at elevated temperatures.[3] As an alternative, methanol oxidative carbonylation has emerged as a promising route to DMC using inexpensive CO, O_2, and methanol as raw materials, generating water as the main byproduct,[5] and proceeding with a highly favorable free energy change ($\Delta G_{298K} = -250.8 \ kJ \cdot mol^{-1}$).[6] The reaction is represented by the following equation

$$CH_3OH + CO + 1/2O_2 \rightarrow DMC + H_2O \tag{1}$$
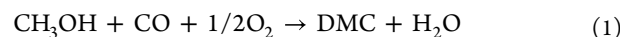
Industrially, methanol oxidative carbonylation is carried out via the ENI process using homogeneous Cu-based catalysts derived from halide copper precursors.[7] The process enables

Table 1. Mechanism of DMC Formation by Methanol Oxidative Carbonylation (* Represents an Active Site)

	elementary steps	E_a (kJ mol^{-1})[38]
O_2 and CH_3OH adsorption	$1/2\ O_2 + * \rightarrow O*$	
	$CH_3OH + * \rightarrow (CH_3OH)*$	
DMC formation path 1	$(CH_3OH)* + O* \rightarrow (CH_3O)*(OH)*$	57.6
	$(CH_3O)*(OH)* + CH_3OH \rightarrow (CH_3O)_2* + H_2O$	54.6
	$(CH_3O)_2* + CO \rightarrow CH_3OCOOCH_3*$	154.8
DMC formation Path 2	$(CH_3OH)* + O* \rightarrow (CH_3O)*(OH)*$	57.6
	$(CH_3O)*(OH)* + CO \rightarrow (CH_3OCOOH)*$	73.5
	$(CH_3OCOOH)* + CH_3OH \rightarrow CH_3OCOOCH_3* + H_2O$	64.5
DMC desorption	$CH_3OCOOCH_3* \rightarrow CH_3OCOOCH_3 + *$	

efficient *in situ* catalyst recycling and achieves a CO_2 footprint (Global Warming Power, GWP 100 years) of 3.18 kg CO_2-eq per kg DMC.[8] However, the use of halides poses challenges such as corrosion of metal equipment and significant environmental burdens including eutrophication, human toxicity, and ecotoxicity across freshwater and terrestrial ecosystems.[8−12]

To address these issues, halogen-free heterogeneous Cu catalysts have been explored, offering the advantages of easier catalyst separation and potentially reduced energy input. Despite these benefits, no commercial heterogeneous process has yet been implemented, primarily due to insufficient catalyst recyclability, which adversely affects both economic viability and environmental impact.

Early efforts to develop heterogeneous Cu catalysts include the work by Bell and co-workers, who prepared Cu-loaded zeolites for methanol oxidative carbonylation. Among the tested materials, Cu−Y zeolite exhibited the highest activity due to the superior accessibility of active Cu centers within the supercage structure, compared to Cu-ZSM-5 and Cu-MOR.[13,14] Pretreatments with acids,[15] bases,[16] or NH_4F[17] were used to open up the faujasite framework, enhancing diffusion. However, DMC selectivity remained below 65% regardless of the pretreatment,[13−17] due to residual Brønsted acid sites that facilitated DMC decomposition and the formation of dimethoxymethane byproducts.[18,19]

More recent developments have focused on carbon-supported Cu catalysts devoid of surface acid species.[10,20] The size of Cu nanoparticles plays a crucial role in determining both activity and stability. For instance, Zhang et al. reported Cu/activated carbon catalysts prepared via the incipient wetness impregnation achieving a DMC space-time yield (STY_{DMC}) of 156 mg·g^{-1}·h^{-1}.[21] Pretreating the carbon support with nitric acid reduced the average size of Cu nanoparticles from 32 to 12 nm, boosting the STY_{DMC} to 229 mg·g^{-1}·h^{-1}. However, severe sintering led to a 45% drop in activity after 120 h on stream.

To enhance stability, various strategies have been explored, including encapsulation within carbon nanosheets[22,23] micropores or mesopores,[22,24−29] and anchoring Cu nanoparticles via coordination with pyridinic nitrogen species.[30−33] Despite these efforts, stability remains a major challenge. For example, anchoring Cu nanoparticles on N-doped graphene (7.5−29.1 nm),[32] hollow carbon spheres (5.5−8.1 nm),[22] or carbon nanotubes (3.0 nm),[26] yielded competitive STY_{DMC} values of 1665, 2504, and 2200 mg·g^{-1}·h^{-1}, respectively. Nonetheless, in all cases, the catalytic performance declined sharply (20−50%) after just 4−6 runs.

The most stable heterogeneous Cu catalyst reported to date was developed by Ren and co-workers, who initially supported

11 nm Cu nanoparticles on N-doped carbon nanosheets.[34] During the reaction, the Cu nanoparticles migrated and became trapped in defect sites, evolving into 0.91 nm clusters and, to a lesser extent, single atoms. This catalyst exhibited STY_{DMC} values between 2197 and 3227 mg·g^{-1}·h^{-1} with 90% DMC selectivity. Catalyst performance proved highly sensitive to the preparation protocol; most formulations exhibited over 37% activity loss after 10 runs. However, by optimizing the synthesis and Cu restructuring process, one catalyst formulation displayed a volcano-shaped activity trend, increasing from 2197 mg·g^{-1}·h^{-1} (1st run) to 2500 mg·g^{-1}·h^{-1} (3rd run), then gradually declining to 2250 mg·g^{-1}·h^{-1} by the 10th run—representing 11% decrease from peak performance. This Cu restructuring was found to occur at temperatures above 100 °C, independent of solvent, atmosphere, pressure, or stirring rate.

There is general agreement that DMC formation from methanol oxidative carbonylation over Cu proceeds via the catalytic mechanism summarized in Table 1. The reaction begins with adsorptive activation of methanol and O_2, forming methoxide species $[(CH_3O)*(OH)*]$. DMC can then form via two primary pathways:[32,35]

In **Path 1**, $(CH_3O)*(OH)*$ reacts with methanol to form dimethoxide species $[(CH_3O)_2*]$, followed by CO insertion to produce DMC. This path is favored over Cu^{2+}, with the rate-limiting step being CO insertion.

In **Path 2**, $(CH_3O)*(OH)*$ reacts with CO to form monomethyl carbonate $[(CH3OCOOH)*]$ that further reacts with methanol to generate DMC. This pathway is dominant over Cu^0 and Cu^+, where the formation of (CH_3OCOOH) is rate-limiting.[36−39] The results point out that Cu^0 and Cu^+ species are more active than Cu^{2+},[10,37,40] where DMC formation is governed by path 2. Theoretical calculations show that the activation barrier of CO insertion on single Cu^0 atom (52.1 kJ·mol^{-1}) and cluster (73.5 kJ mol^{-1}) is lower than on Cu^0(111) in a nanoparticle (92 kJ·mol^{-1}).[41]

In summary, both theoretical and experimental studies demonstrate that the catalytic performance and stability of Cu-based catalysts in methanol oxidative carbonylation is strongly influenced by the size and oxidation state of the Cu species. Confining Cu to single atoms or small clusters is expected not only to enhance catalytic activity but, more importantly, to significantly improve stability due to strong chemical bonding between the isolated Cu sites and the support.

Zeolitic Imidazole Frameworks (ZIFs) offer a promising platform for the synthesis of highly dispersed metal catalysts, including those with atomic-scale metal distribution.[42] Co-doped ZIF-8 and ZIF-67 have been employed as sacrificial templates to prepare Co catalysts supported on carbon and carbon nitride through pyrolysis.[43−45] In this strategy, Zn^{2+}

Scheme 1. Illustration of Cu$_x$-ZIF-8 Precursor and Cu$_x$/NC Catalyst Preparation
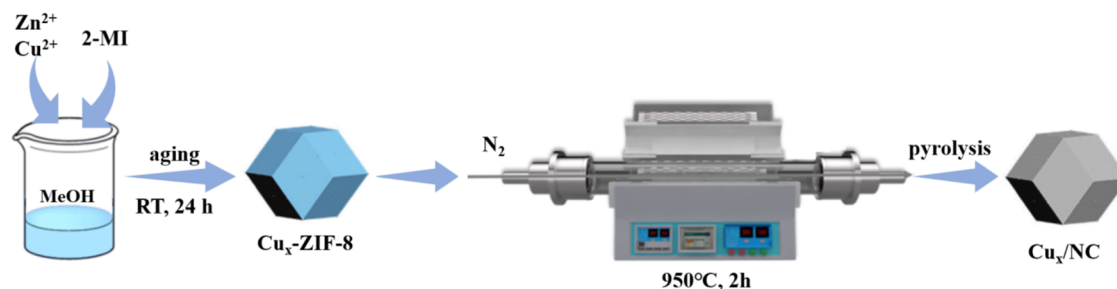
ions in the parent ZIF structure serve as spacers that promote metal dispersion. Upon pyrolysis, Zn metal readily evaporates (boiling point: 907 °C), leaving behind Zn^{2+} vacancies that create noncoordinated nitrogen sites capable of anchoring metal atoms introduced via impregnation or *in situ* synthesis.[46,47] These sites discourage nanoparticle aggregation and favor the formation of isolated atoms or clusters. This methodology has previously been explored for Cu-based systems, though the resulting catalysts often exhibit very low Cu loadings (<2.28 wt %).[48] On the other hand, excessive Cu loading (>50 mol %) in the ZIF-8 precursor can lead to structural collapse of the framework.[49]

Herein, we report a robust and reproducible method for preparing single-atom and cluster-like Cu species supported on N-doped carbon (NC) via pyrolysis of Cu-ZIF-8 precursors. Detailed structural and chemical characterization of the catalysts was carried out using X-ray diffraction (XRD), Fourier transform infrared (FT-IR), high-resolution transmission electron microscopy (HR-TEM), aberration corrected high angle annular dark field-scanning transmission electron microscopy (AC-HAADF-STEM), X-ray photoelectron spectroscopy (XPS), NH$_3$-TPD, H$_2$-TPR, and X-ray absorption spectroscopy (XAS). The catalysts were evaluated in the liquid-phase methanol oxidative carbonylation to DMC to investigate how the dispersion and coordination environment of Cu influence activity, selectivity, and stability—particularly in terms of resistance to leaching, sintering, and over-oxidation—compared to conventional supported Cu nanoparticle catalysts. The best catalyst exhibits exceptional stability and recyclability, maintaining high activity and selectivity for DMC over multiple catalytic runs.

2. EXPERIMENTAL SECTION

2.1. Materials. Copper(II) nitrate trihydrate (Cu(NO$_3$)$_2$·3H$_2$O, 99%), zinc nitrate hexahydrate (Zn(NO$_3$)$_2$·6H$_2$O, 99%), 2-methyl-imidazole (97%), methanol (99.5%), and ethanol (99.7%) were purchased from Chengdu Chron Chemicals Reagent Co., Ltd. Nitrogen (N$_2$, 99.99%) and oxygen (O$_2$, 99.99%) were supplied by Sichuang Qiaoyuan Gas Co., Ltd. Carbon monoxide (CO, 99.99%) was obtained from Chongqing Kaiyi Special Gas Co., Ltd. All chemicals and gases were used as received without further purification.

2.2. Preparation of Cu$_x$/NC Catalysts. The synthesis of the copper-supported N-doped carbon catalysts (Cu$_x$/NC) involved two steps, as illustrated in Scheme 1: (1) solvothermal synthesis of the Cu$_x$-ZIF-8 precursors, and (2) pyrolysis to yield Cu$_x$/NC catalysts.

2.2.1. Preparation of Cu$_x$-ZIF-8 Precursors. A given amount of Cu(NO$_3$)$_2$·3H$_2$O and Zn(NO$_3$)$_2$·6H$_2$O [total metal content = 20 mmol, Cu^{2+}/(Cu^{2+} + Zn^{2+}) = 0, 0.1, 0.2, 0.3, 0.4] was dissolved in 280 mL of methanol. In parallel, 160 mmol of 2-methylimidazole (2-MI) were dissolved in another 280 mL of methanol. Both solutions were mixed, stirred for 1 h, and then aged at room temperature for 24 h.

The resulting solid was separated by centrifugation, washed five times with methanol, and dried at 60 °C overnight. The samples were denoted as Cu$_{0.0}$-ZIF-8, Cu$_{0.1}$-ZIF-8, Cu$_{0.2}$-ZIF-8, Cu$_{0.3}$-ZIF-8 and Cu$_{0.4}$-ZIF-8, according to the Cu loading.

2.2.2. Preparation of Cu$_x$/NC. Each Cu$_x$-ZIF-8 precursor was placed in a quartz boat and pyrolyzed in a tube furnace under N$_2$ atmosphere. The temperature was increased to 950 °C at a rate of 5 °C·min^{-1}, held for 2 h, and then cooled to room temperature. The resulting catalysts were denoted as Cu$_{0.0}$/NC to Cu$_{0.4}$/NC, in correspondence with the precursor composition.

2.3. Catalyst Characterization. The bulk Cu and Zn content in the catalysts was measured by Inductively Coupled Plasma Optical Emission Spectrometer (ICP-OES, Agilent 700 Series ICP-OES). Before the tests, the catalysts were calcined in air atmosphere at 600 °C for 2 h and then dissolved in nitric acid.

The crystal phases in the catalysts were investigated by powder X-ray diffraction (XRD, DX-2700BH) using Cu Kα radiation (λ = 1.5406 Å) with a scan rate of 2 °C·min^{-1} and a step length of 0.01°.

Fourier transform infrared spectra (FT-IR) were performed on a Thermo Scientific FTIR-Nicolet iS50 spectrometer to identify all functional groups.

The morphology of the catalysts was investigated using field emission scanning electron microscope (FESEM, ZEISS Sigma 300). Transmission electron microscope (TEM, JEOL JEM-F200), aberration corrected high angle annular dark field-scanning transmission electron microscopy (AC-HAADF-STEM, FEI Titan G2 60–300), and energy-dispersive X-ray spectroscopy (EDS) mapping were used to assess the surface distribution of Cu and Zn on the catalysts.

N$_2$ adsorption–desorption isotherms of the samples were measured on a Bjbuilder SSA-4000 adsorption apparatus at −196 °C. Before the tests, the catalysts were degassed at 150 °C for 12 h to remove moisture and adsorbed vapors.

X-ray photoelectron spectroscopy (XPS) analyses carried out on a Thermo Scientific K-α apparatus using the Al Kα line as excitation source. The binding energy was calibrated using adventitious C 1s carbon appearing at 284.6 eV, and the background was deducted by the Smart method. The Cu and Zn surface content was measured from the survey spectra.

The H$_2$ temperature-programmed reduction (H$_2$-TPR) profiles of the catalysts were measured on a Bjbuilder PCA-1200 adsorption apparatus. First, 50 mg of the given catalyst was purged under He flow [30 mL(STP)·min^{-1}] at 180 °C for 1 h. After cooling, the temperature was raised to 700 °C (5 °C·min^{-1}) in 5% H$_2$/N$_2$ at a flow rate of 30 mL(STP)·min^{-1} and the real-time signal was recorded using a TCD detector. The H$_2$ uptake was measured from the H$_2$-TPR profiles by integrating the bands in the temperature range between 120 and 260 °C, $\Phi_{H_2}(120 \rightarrow 260)$, and normalized against the bulk Cu composition using the expression

$$\text{H}_2 \text{ uptake} = \frac{\Phi_{H_2}(120 \rightarrow 260)\ (\text{mol H}_2/\text{g})}{\text{bulk Cu content (wt \%)}} \quad (2)$$

The NH$_3$ temperature-programmed desorption (NH$_3$-TPD) profiles of the catalysts were measured on the same instrument. After purging under He flow [30 mL(STP)·min^{-1}] at 180 °C for 1 h, a 3% NH$_3$/N$_2$ flow 30 mL(STP)·min^{-1} was adsorbed at 60 °C for 30

min, and then purged with He for 20 min. Finally, the temperature was raised to 700 °C at a rate of 5 °C·min⁻¹ and the real-time signal was recorded using a TCD detector.

X-ray absorption spectroscopy (XAS) measurements were conducted at beamline I20-scanning at Diamond Light Source Ltd., Didcot U.K. (proposal NT40509−1). The storage ring was operated with an electron current of 300 mA at 3 GeV. I20-scanning produces radiation from a wiggler source in combination with a cryogenically cooled four-bounce Si(111) monochromator (photon flux *ca.* 1×10^{12} ph·s⁻¹). A pair of Rh coated focusing mirrors were used to focus the beam to *ca.* $400 \times 300 \ \mu m^2$ (H × V FWHM) at the sample position, and higher order harmonics from the monochromator were removed using the Rh stripe of the available harmonic rejection mirror system at an incidence angle of 5.0 mrad. The beam was attenuated using 0.2 mm Al, which was found to prevent any spectral changes over the acquisition period. The monochromator energy was calibrated using a reference Cu metal foil by setting the first inflection point of the Cu K edge to be 8979 eV. Samples were prepared as 13 mm pressed pellets and measured in transmission mode. The incident and transmitted beam through the sample were measured using two 30 cm long ion chambers optimized using a He−Ar gas mixture to absorb 15 and 80% of the beam, respectively. Two scans per sample were collected with energy steps of 5 eV (8779−8948 eV) and 0.3 eV (8948−8966 eV) with a time step of 1 s·step⁻¹, and 0.04 Å⁻¹ (8966−9720 eV) with a variable time step of 1−3 s·step⁻¹ in this region. Extended X-ray absorption fine structure (EXAFS) fitting was performed using the Artemis program within the Demeter package. Two paths were used to perform the single shell fit of the data: a Cu−Cu path and a generated Cu−N path (1.95 Å). The amplitude reduction factor S_0^2 for each fit was fixed to that of the collected metallic Cu foil (0.78), with the degeneracy, N, being given as the product of S_0^2 and n. The variable n was used to account for the reduction in average coordination number for the present nanoparticulate Cu species. All other parameters (σ^2, N and ΔE_0) were considered as free parameters during the fit, which was performed over the 1−3 Å region of the Fourier transformed data in real space.

2.4. Evaluation of the Catalytic Performance. The methanol oxidative carbonylation tests on the different catalysts were carried out in a 100 mL high-pressure kettle with magnetic stirring. The kettle was charged with 0.1 g of catalyst and 10 mL of methanol, purged with CO, then pressurized with 3.6 MPa CO and 0.4 MPa O₂. Stirring was maintained at 300 rpm to eliminate mass transfer limitations according to preliminary experiments. The temperature was raised to 120 °C over 30 min and held for 2 h. After cooling, the catalyst was removed by centrifugation, and the supernatant was analyzed by gas chromatography (FULI GC 9790, SE-54 column, FID detector).

The methanol conversion (C_{MeOH}), selectivity to DMC (S_{DMC}), methyl formate (S_{MF}), dimethoxy methane (S_{DMM}), and space-time yield of DMC (STY_{DMC}), and turnover frequency at time zero expressed as a function of the bulk Cu content ($TOF_{DMC,B}$) and surface Cu content ($TOF_{DMC,S}$) were computed using the following expressions

$$C_{MeOH} = \frac{n_{reaction\,methanol} \ (mol)}{n_{total\,methanol} \ (mol)} \times 100\% \tag{3}$$

$$S_{DMC} = \frac{2n_{DMC} \ (mol)}{n_{reaction\,methanol} \ (mol)} \times 100\% \tag{4}$$

$$S_{MF} = \frac{2n_{MF} \ (mol)}{n_{reaction\,methanol} \ (mol)} \times 100\% \tag{5}$$

$$S_{DMM} = \frac{3n_{DMM} \ (mol)}{n_{reaction\,methanol} \ (mol)} \times 100\% \tag{6}$$

$$STY_{DMC} = \frac{m_{DMC} \ (mg)}{m_{cat} \ (g) \times t \ (h)} \tag{7}$$

$$TOF_{DMC,B} = \frac{STY_{DMC} \times M_{Cu}}{M_{DMC} \times \omega} \tag{8}$$

$$TOF_{DMC,S} = \frac{STY_{DMC} \times M_{Cu}}{M_{DMC} \times \omega \times D_{Cu} \times X} \tag{9}$$

where D_{Cu} is the Cu dispersion measured by HR-TEM and AC-HAADF-STEM, ω is the bulk Cu content in the catalyst, X is the surface percentage of Cu⁰ + Cu⁺ measured by XPS, and M_{DMC} and M_{Cu} are the molar weight of DMC (90.1 g·mol⁻¹) and Cu (63.5 g·mol⁻¹), respectively. The relative error of the STY_{DMC} measurements was estimated at 3% by performing selective replicate measurements on the different catalysts.

Given the enrichment of Cu single atoms and clusters on the most active catalyst samples, making them not suitable for standard chemisorption methods (e.g., N₂O surface oxidation + further H₂-TPR surface reduction),[22,30] D_{Cu} was measured directly from HR-TEM and AC-HAADF-STEM using the expression

$$D_{Cu} = D_{Cu,S} \times \frac{\omega_S}{\omega} \tag{10}$$

where $D_{Cu,S}$ is the dispersion measured against the surface-to-bulk ratio of Cu in the samples, ω_S. $D_{Cu,S}$ was assumed to approach 100% for samples with Cu single atoms and clusters,[50,51] whereas it was computed from the following expression for samples enriched with supported Cu nanoparticles/large clusters

$$D_{Cu,S} = 6\frac{M_{Cu}}{\rho_{Cu}} \frac{1}{N_A \times \pi r_{Cu}^2} \frac{1}{d_p} \tag{11}$$

where ρ_i is the Cu density, N_A is the Avogadro Number, r_i is the covalent radius of Cu and d_p is the average size of Cu particles measured by HR-TEM and AC-HAADF-STEM by assuming that metal particles are spherical in shape. The average particle size (surface weighted, $d_p[3,2]$) was estimated from the particle size distribution using the expression

$$d_p[3, 2] = \frac{\sum_{i=1}^{i=n} d_{p,i}^3 n_i}{\sum_{i=1}^{i=n} d_{p,i}^2 n_i} \tag{12}$$

In some experiments, the spent catalyst was separated from the reactor, vacuum-dried at 60 °C for 2 h, and tested in consecutive runs to evaluate its stability against Cu sintering, overoxidation and hydration. The catalyst deactivation was computed from the space-time yield after the first and n runs, i.e., $(STY_{DMC})_1$ and $(STY_{DMC})_n$, respectively, as follows

$$deactivation = 1 - \frac{(STY_{DMC})_n}{(STY_{DMC})_1} \tag{13}$$

The error of catalyst deactivation was estimated by propagating the error from eq 14. Considering the relative error for both $(STY_{DMC})_1$ and $(STY_{DMC})_n$ (3%) as measured experimentally from the standard deviation of 5 catalytic tests, the error of catalyst deactivation reads as follows

$$Error_{deactivation} = \sqrt{2}\left[\frac{(STY_{DMC})_n}{(STY_{DMC})_1}\right](0.03) \tag{14}$$

3. RESULTS AND DISCUSSION

3.1. Preparation and Characterization of Cu$_x$-ZIF-8 Catalyst Precursors. Five different Cu$_x$-ZIF-8 samples were synthesized by mixing solutions of Zn(NO₃)₂, Cu(NO₃)₂ and 2-MI at room temperature with varying Cu²⁺/(Cu²⁺+Zn²⁺) molar ratios. The Cu weight contents determined by ICP-OES are 0.00, 0.66, 1.20, 1.89, and 2.32%, while the Zn weight contents slightly decrease from 27.99 to 26.02% (Table S1),
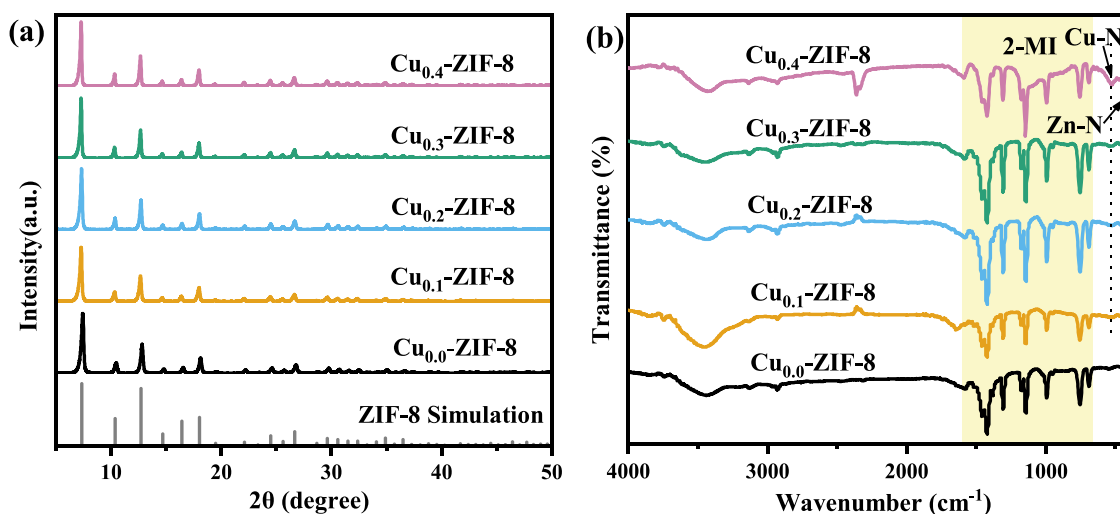
Figure 1. (a) XRD patterns and (b) FT-IR spectra of Cu_x-ZIF-8 precursors.

Table 2. Bulk and Surface Cu and Zn Content and Textural Properties of Cu_x/NC Catalysts

					bulk content[d]			surface content[e]			surface vs bulk[d,e]	
catalyst	S_{BET} $(m^2 \cdot g^{-1})$[a]	average Cu size (nm)[b]	$D_{Cu,S}$ (%)[b]	H_2 uptake $(mmol \cdot g_{Cu}^{-1})$[c]	Zn (wt %)	Cu (wt %)	Zn/Cu (mol/mol)	Zn (wt %)	Cu (wt %)	Zn/Cu (mol/mol)	Zn_{surf}/Zn_{bulk} (mol/mol)	Cu_{surf}/Cu_{bulk} (mol/mol)
$Cu_{0.0}$/NC	1023				0.21	0		3.60	0			
$Cu_{0.1}$/NC	938	0.49	100	0.25	0.16	2.98	0.052	3.24	1.93	1.68	20.3	0.65
$Cu_{0.2}$/NC	1191	0.56	100	4.44	0.26	6.73	0.037	3.09	2.03	1.52	11.9	0.30
$Cu_{0.3}$/NC	977	1.18	20	6.27	0.37	9.11	0.039	3.13	1.79	1.75	8.50	0.20
$Cu_{0.4}$/NC	907	1.75	21	6.24	0.17	12.77	0.013	2.68	2.08	1.29	15.8	0.16

[a]Measured by N_2 adsorption−desorption at −196 °C. [b]Only Cu clusters/nanoparticles, measured by TEM (surface); Cu dispersion measured using for nanoparticles >5 nm for $Cu_{0.3}$/NC and $Cu_{0.4}$/NC. [c]Measured by H_2-TPR in the temperature range 120−260 °C. [d]Measured by ICP-OES. [e]Measured by XPS from survey spectra.

closely matching the theoretical Zn content in pristine ZIF-8 (28.47%).

X-ray diffraction (XRD) patterns (Figure 1a) confirm that all Cu_x-ZIF-8 samples retained the characteristic reflections of the ZIF-8 framework, consistent with earlier studies.[52,53] The preservation of the body-centered cubic structure suggests that Cu doping does not distort the lattice, likely due to the similar ionic radii of Cu^{2+} (0.72 Å) and Zn^{2+} (0.74 Å). No peaks corresponding to Cu^0, Cu_2O, or CuO were observed, indicating complete incorporation of Cu into the framework or a high dispersion of surface or bulk Cu species.

FT-IR spectroscopy (Figure 1b) reveals consistent vibrational features across all samples, matching the signatures of the 2-MI linker.[53,54] Characteristic bands are visible at 692 cm^{-1} (C−H bending), 760 cm^{-1} (C−H bending), 995 cm^{-1} (=C−H in-plane bending), 1147 cm^{-1} (=C−H in-plane deformation), 1307 cm^{-1} (CH_2 bending), 1383 cm^{-1} (CH_3 bending), 1425 cm^{-1} (CH_2 bending), 1456 cm^{-1} (C=C stretching) and 1585 cm^{-1} (C=N stretching). A band at 423 cm^{-1} corresponds to Zn−N vibrations,[55] while a new band at 540 cm^{-1}, observed in all Cu-doped samples, is attributed to Cu−N stretching.[55,56] This supports the incorporation of Cu^{2+} within the ZIF framework. A broad band near 3500 cm^{-1} is attributed to adsorbed water within ZIF-8 micropores.

SEM images (Figure S1) show that all samples exhibit rhombohedral dodecahedral morphology with uniform particle dispersion. Particle size increases from 58 to 259 nm with increasing Cu content (Table S1). The particle growth

mechanism likely involves fewer nucleation sites as Zn^{2+} content decreases, resulting in larger crystal sizes.[49]

N_2 adsorption−desorption measurements at −196 °C (Figure S2a) reveal isotherms combining Type I and IV characteristics, indicative of micropores and interparticle meso/macropores (~80 nm, Figure S2b). Specific surface areas range between 1442 and 1557 $m^2 \cdot g^{-1}$ (Table S1), suggesting that Cu doping does not significantly alter pore architecture.

3.2. Preparation and Characterization of Cu_x/NC Catalysts. 3.2 1. Textural Properties. Five Cu_x/NC catalysts were prepared via pyrolysis of the corresponding Cu_x-ZIF-8 precursors. N_2 adsorption−desorption isotherms at −196 °C (Figure S3a) show similar profiles to the precursors, with a notable hysteresis loop in the medium pressure range ($P/P_0 = 0.4−0.7$), indicating mesopore formation (2−10 nm, Figure S3b). Compared to the precursors, the density of <10 nm mesopores increases postpyrolysis, while macropore size and volume remain largely unchanged.

This mesoporosity enhancement is attributed to partial collapse of ZIF frameworks during pyrolysis, especially with higher Cu content, which reduces structural stability.[53] Specific surface areas range from 907 to 1192 $m^2 \cdot g^{-1}$ (Table 1), remaining comparable despite the generation of mesopores. This is likely due to simultaneous loss of micropores, which dominate the surface area. The high surface area and hierarchical micromeso-macroporosity are expected to facilitate reactant diffusion and improve accessibility to Cu active sites.[57] SEM images (Figure S4) confirm that all Cu_x/NC
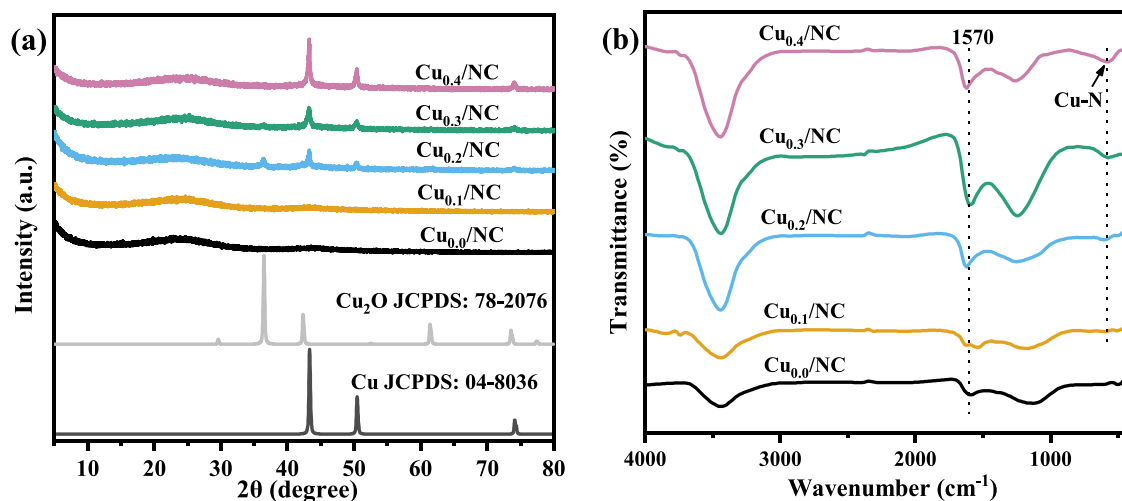
Figure 2. (a) XRD patterns and (b) FT-IR spectra of Cu_x/NC catalysts.
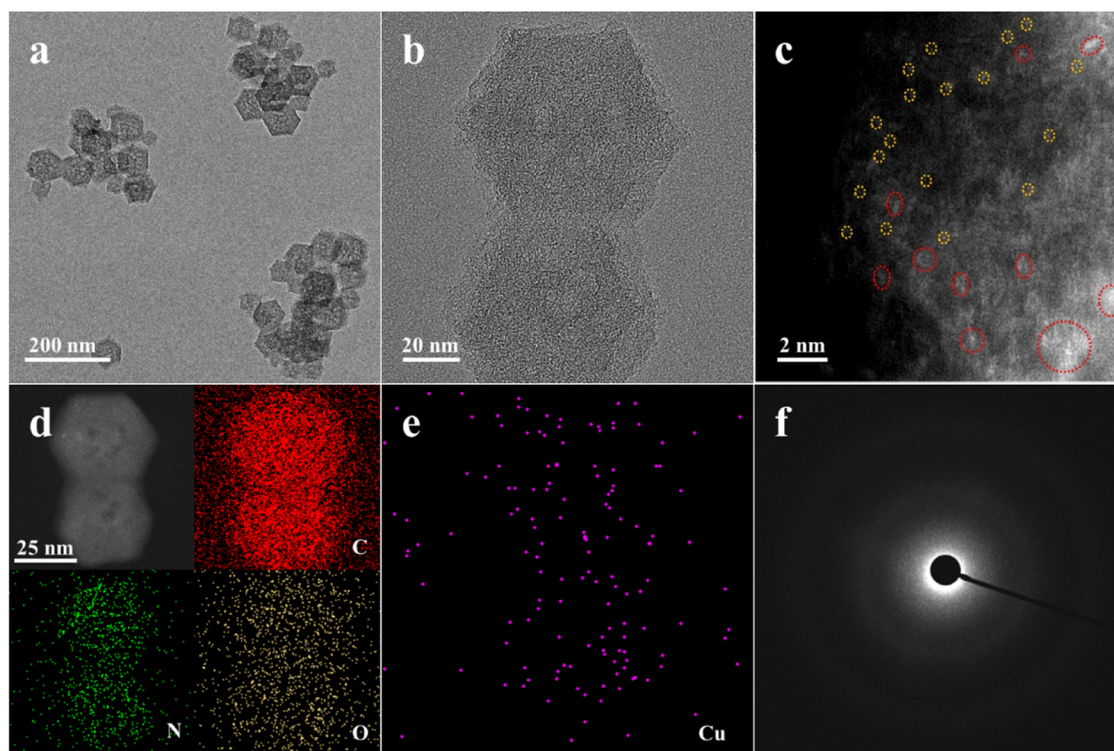
Figure 3. (a, b) TEM micrographs, (c) AC-HAADF-STEM micrograph, (d, e) STEM-EDS elemental mapping, and (f) SAED pattern of an individual rhomboid dodecahedron of $Cu_{0.2}/NC$.

catalysts retain the rhombohedral dodecahedral morphology of Cu_x-ZIF-8 precursors.

3.2 2. Bulk Cu Composition and Speciation. ICP-OES analysis (Table 2) shows that bulk Cu content increases with nominal Cu precursor loading, ranging from 2.98 wt % ($Cu_{0.1}/$ NC) to 12.77 wt % ($Cu_{0.4}/NC$). In contrast, Zn content remains nearly constant (0.16−0.37 wt %), suggesting that approximately 98% of Zn volatilizes during pyrolysis.

The bulk Zn/Cu molar ratio decreases monotonously from 0.052 ($Cu_{0.1}/NC$) to 0.037−0.039 ($Cu_{0.2}/NC$, $Cu_{0.3}/NC$), and 0.013 ($Cu_{0.4}/NC$), much lower than in the precursors (11−40), confirming significant Zn loss during pyrolysis (>98%). At lower Cu loadings ($Cu_{0.1}/NC$ to $Cu_{0.3}/NC$), Cu appears to partially occupy the Zn vacancies. For higher Cu

content ($Cu_{0.4}/NC$), excess Cu likely resides elsewhere within the NC matrix or on the surface.

XRD patterns (Figure 2a) of all Cu_x/NC catalysts, regardless of Cu loading, show a broad peak at ∼26°, characteristic of graphitic carbon (002), indicating complete graphitization during pyrolysis.[58] No reflections from the Cu_x-ZIF-8 precursors are detected. A weak peak at 36.4° in $Cu_{0.2}/NC$ and $Cu_{0.3}/NC$ corresponds to $Cu_2O(111)$ facets (JCPDS: 78− 2076), with an estimated abundance below 5%. Additional reflections at 43.3, 50.5 and 74.2°, corresponding to $Cu^0(111)$, $Cu^0(200)$, and $Cu^0(220)$ (JCPDS: 04−0836), are observed for $Cu_{0.2-0.4}/NC$ samples, increasing in intensity with Cu content. In $Cu_{0.2}/NC$, these peaks are weak (<10% relative to a reference Cu^0 sample), while $Cu_{0.3}/NC$ and $Cu_{0.4}/NC$ show
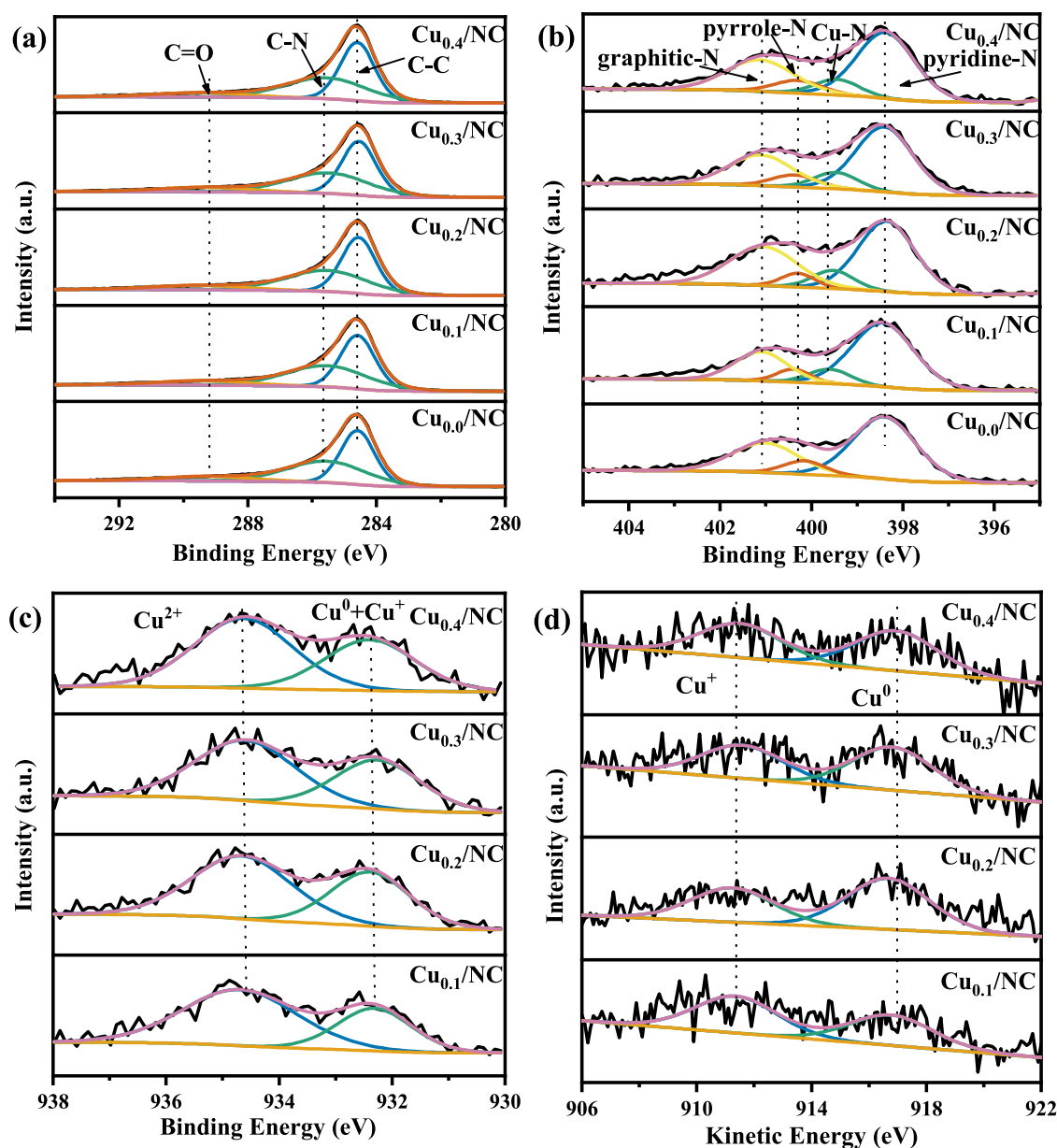
Figure 4. (a) C 1s, (b) N 1s, (c) Cu 2p$_{3/2}$ XPS and (d) Cu LMM Auger spectra of Cu$_x$/NC catalysts.

more pronounced signals. No Cu-related reflections are detected in Cu$_{0.1}$/NC, suggesting atomically dispersed Cu or ultrasmall clusters. Absence of ZnO-related peaks implies ZnO, if present, is highly dispersed or amorphous.

FT-IR spectra (Figure 2b) confirm the complete carbonization of the imidazole ligand, with disappearance of its characteristic bands. A broad band at 1570 cm^{-1} is attributed to overlapping C=C and C=N bands in the carbon matrix.[47] The Zn−N vibration at 423 cm^{-1} vanishes postpyrolysis, while the Cu−N band at 540 cm^{-1} persists, indicating Zn volatilization leads to nitrogen vacancies that coordinate Cu atoms. NH$_3$-TPD profiles (Figure S5) show no desorption peaks, confirming the absence of medium or strong acid sites and the elimination of noncoordinated Zn^{2+} species. A broad FT-IR band centered at 3500 cm^{-1}, attributed to adsorbed water, increases with Cu content.

3.2 3. Catalyst Reducibility. The reducibility of Cu$_x$/NC catalysts was evaluated by H$_2$-TPR (Figure S6). Cu$_{0.2}$/NC and Cu$_{0.3}$/NC display a complex reduction profile below 250 °C,

which can be deconvoluted into two bands attributed to the sequential reduction of CuO and Cu$_2$O to Cu^0.[26] Cu$_{0.4}$/NC shows a single band, corresponding solely to CuO reduction, consistent with the absence of Cu$_2$O reflections in the XRD patterns. Cu$_{0.1}$/NC exhibits only a weak reduction signal, likely due to its low Cu content. The main reduction peak shifts from 164 °C (Cu$_{0.2}$/NC) to 206 °C (Cu$_{0.4}$/NC), indicating stronger metal−support interactions at higher Cu loadings, possibly due to partial encapsulation of Cu species (*vide infra*).[26]

H$_2$ uptake (120−260 °C, Table 2) increases with Cu content: from 0.25 mmol·gCu^{-1} (Cu$_{0.1}$/NC) to 4.44 mmol·gCu^{-1} (Cu$_{0.2}$/NC), reaching ~6.3 mmol·gCu^{-1} for Cu$_{0.3}$/NC and Cu$_{0.4}$/NC. These values suggest greater Cu^0 abundance and/or stronger interactions between Cu species (atoms, clusters, or nanoparticles) and the support, particularly for highly dispersed Cu in Cu$_{0.1}$/NC. The observed reducibility trends are attributed to electron transfer from organic ligands to Cu^{2+} during pyrolysis and a higher oxidation state of surface Cu species in the final catalysts.

G

Table 3. Cu and N Speciation over Cu_x/NC Catalysts

catalyst	surface Cu content (mol %)[a]			surface N content (mol %)[b]			
	Cu^0	Cu^+	Cu^{2+}	pyridine-N	Cu−N	pyrrole-N	graphitic-N
$Cu_{0.0}/NC$				60.5		8.8	30.7
$Cu_{0.1}/NC$	14.9	18.0	67.1	61.3	6.1	8.0	24.5
$Cu_{0.2}/NC$	24.2	16.2	59.5	51.5	10.8	7.7	29.9
$Cu_{0.3}/NC$	22.9	17.9	59.2	52.9	10.6	6.3	30.2
$Cu_{0.4}/NC$	21.7	18.4	59.9	49.5	9.9	6.4	34.2

[a]Measured by XPS ($Cu\ 2p_{3/2}$). [b]Measured by XPS (N 1s).

3.2.1. Oxidation State and Dispersion of Cu Species. The internal morphology of Cu_x/NC catalysts was investigated by HR-TEM (Figures 3 and S7−S9). $Cu_{0.1}/NC$ and $Cu_{0.2}/NC$ display highly dispersed Cu species, with $Cu_{0.1}/NC$ containing only isolated single atoms (average size: 0.49 nm), and $Cu_{0.2}/NC$ containing both single atoms and small clusters (average size: 0.56 nm) (Table 2). No large Cu nanoparticles are observed in either sample (Figures 3a,b and S7a,b). Although XRD reveals Cu^0 and Cu_2O phases in $Cu_{0.2}/NC$, their absence in TEM suggests partial encapsulation of these nanoparticles within the carbon matrix.

In contrast, Cu nanoparticles are clearly visible on the surfaces of $Cu_{0.3}/NC$ and $Cu_{0.4}/NC$ (Figures S8a and S9a), with average sizes of 1.18 and 1.75 nm, respectively, and maximum diameters reaching 5 nm and 10 nm. HR-TEM images of $Cu_{0.3}/NC$ and $Cu_{0.4}/NC$ (Figures S8b and S9b) reveal lattice fringes with a spacing of 0.21 nm, corresponding to $Cu^0(111)$ lattice planes, consistent with XRD data.[59]

To elucidate the Cu dispersion, $Cu_{0.2}/NC$ was imaged by AC-HAADF-STEM (Figure 3c). Based on differences in atomic numbers, AC-HAADF-STEM has proven to be an efficient technique to visualize isolated, heavier Cu on carbon supports.[60] AC-HAADF-STEM imaging of $Cu_{0.2}/NC$ (Figure 3c) confirms the presence of isolated single atoms (yellow) and small clusters (red), without evidence of nanoparticle formation. Elemental mapping (C, N, O, Cu) and SAED analysis (Figure 3d−f) further confirm uniform Cu dispersion, which is similarly observed in $Cu_{0.1}/NC$ (Figure S7d,e). Conversely, elemental maps of $Cu_{0.3}/NC$ and $Cu_{0.4}/NC$ (Figures S8d and S9d) show distinct Cu nanoparticle domains. Corresponding SAED patterns (Figures S8e and S9e) display diffraction spots characteristic of crystalline Cu, confirming the presence of surface-exposed Cu^0 nanoparticles. STEM-EDS mapping (Figure S10) reveals no spatial overlap between Cu and Zn, confirming the absence of Cu−Zn alloy formation across all catalysts.

It is well-established that metal surface energy increases with decreasing particle sizes, promoting sintering.[61] A common strategy to inhibit sintering is to enhance the spatial separation between metal atoms on the support. In Cu_x-ZIF-8, Cu atoms are initially isolated by neighboring Zn nodes, which weakens Cu−Cu interactions. During pyrolysis, Zn volatilizes, leaving N-vacancies that can anchor Cu species. However, in $Cu_{0.3}/NC$ and $Cu_{0.4}/NC$, insufficient Zn-mediated isolation and reduced interparticle spacing at higher Cu loadings may lead to Cu agglomeration and sintering.[43,62]

XPS analysis confirms the presence of C, N, O, Cu, and Zn in all catalysts (Figure S11a,b). High-resolution C 1s spectra (Figure 4a) reveal peaks at 284.8, 285.7, and 289.4 eV, corresponding to C−C, C−N, and C═O groups.[63] N 1s spectra (Figure 4b) display four components at 398.3, 399.4, 400.3, and 401.0 eV, assigned to pyridinic-N, Cu−N, pyrrolic-

N, and graphitic-N, respectively.[63,64] $Cu\ 2p_{3/2}$ spectra (Figure 4c) show two peaks at 934.6 eV and 932.3 eV, attributed to Cu^{2+} and a combination of Cu^+/Cu^0, respectively.[21,65,66] Further discrimination between Cu^0 and Cu^+ was achieved via Cu LMM Auger spectra: peaks at 911.5 eV and 916.8 eV correspond to Cu^+ and Cu^0, respectively.[34] The $Zn\ 2p_{3/2}$ spectra (Figure S11c) exhibit a single band centered at 1021.8 eV, consistent with ZnO.[67]

XPS analysis of Cu_x/NC catalysts (Table 2) reveals that surface Zn content decreases progressively with increasing bulk Cu loading, from 3.60 wt % (Cu_0/NC) to 2.68 wt % ($Cu_{0.4}/NC$). In contrast, surface Cu content increases from 1.93 wt % ($Cu_{0.1}/NC$) to 2.08 wt % ($Cu_{0.4}/NC$). Consequently, the surface Zn/Cu molar ratio declines from 1.68 to 1.29 across the series. These values are significantly higher than bulk Zn/Cu ratios measured by ICP-OES (0.013−0.052), indicating surface Zn enrichment. This may arise from Zn redeposition following volatilization during pyrolysis or from bulk-to-surface migration.

Surface-to-bulk Cu ratios are <1 for all samples (0.65, 0.30, 0.20, and 0.16 for $Cu_{0.1−0.4}/NC$), suggesting encapsulation of Cu species. This encapsulation likely results from the inward diffusion of Cu into Zn-deficient regions formed during Zn leaching,[68] consistent with XRD evidence of encapsulated Cu nanoparticles (Figure 2a).

High-resolution XPS of N 1s and Cu 2p regions (Table 3) confirms the presence of pyridinic-N, Cu−N, pyrrolic-N, and graphitic-N species across all catalysts. Pyridinic-N decreases with Cu loading (61% to 50%), while graphitic-N increases (25 to 34%), indicating N-structure evolution during pyrolysis. Cu−N coordination increases from 6.1 to 10%, suggesting enhanced anchoring of Cu species at higher loadings.

Cu speciation remains relatively consistent across samples, with Cu^{2+} as the dominant surface species. The surface proportion of Cu^{2+} decreases from 67% ($Cu_{0.1}/NC$) to 60% ($Cu_{0.4}/NC$), with a corresponding increase in Cu^0. The enrichment in Cu^{2+} is likely due to partial surface oxidation of Cu^0 upon air exposure.[69]

X-ray absorption spectroscopy (XAS) was employed to probe the oxidation state and coordination environment of Cu in $Cu_{0.1}/NC$, $Cu_{0.2}/NC$, and $Cu_{0.2}/NC\_spent$ (Figure 5). The normalized XANES spectra (after background subtraction) and their derivatives reveal a distinct pre-edge feature (A) at 8977.0 eV for $Cu_{0.1}/NC$ and $Cu_{0.2}/NC$, attributed to 1s → 3d transitions in Cu^{II} with partially filled $3d_{x^2−y^2}$ orbitals in centrosymmetric environments.[70,71] This feature is absent in fully occupied d^{10} systems such as Cu_2O.

$Cu_{0.1}/NC$ uniquely exhibits a feature, distinct from $Cu_{0.2}/NC$, at 8980.8 eV labeled (C), corresponding to a 1s → 4p transition that has been reported for both Cu_2O and Cu^{II} nitrosobenzene complexes.[70] We assign this feature to Cu^{II} in a centrosymmetric environment (e.g., planar), as this is also
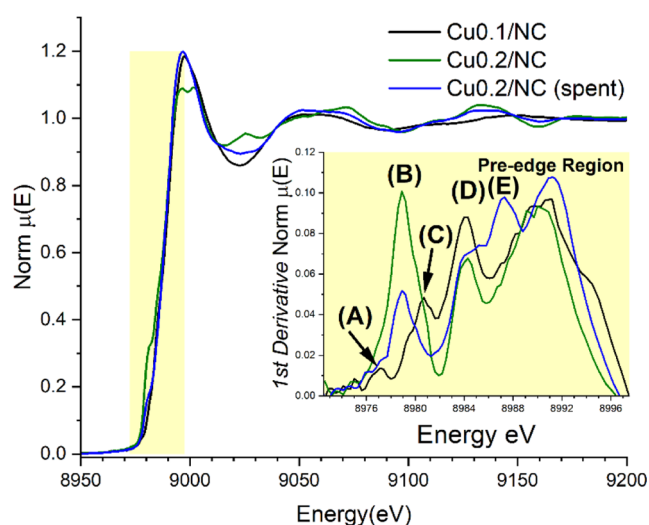
Figure 5. Near-edge structure (XANES) for samples $Cu_{0.1}/NC$, $Cu_{0.2}/NC$ and $Cu_{0.2}/NC\_spent$.

supported by the EXAFS fitting (*vide infra*) and Cu_2O nanoparticles. The latter, being detected by XRD but with very low abundance, are expected to be encapsulated within the NC particles.

Both $Cu_{0.1}/NC$ and $Cu_{0.2}/NC$ exhibit a feature at 8984.2 in the derivative spectrum labeled as (D) that is likely attributed to metallic Cu^0.[72,73] An additional feature located at 8979.0 eV, labeled as (B), is observed for $Cu_{0.2}/NC$ that might also correspond to 1s → 4p transitions in Cu^0,[73,74] but not at the higher energies reported for Cu^I complexes,[75] which may also produce the splitting of the white line feature at 8998.6 eV.

Overall, Cu in $Cu_{0.1}/NC$ is predominantly in the Cu^{II} oxidation state with planar coordination and minimal metallic content. In contrast, $Cu_{0.2}/NC$ exhibits a mixed-valence state, including both Cu^{2+} and Cu^0 species, indicating increased metallic character with higher Cu loading.

Figure 6 displays the experimental and fitted EXAFS spectra, with fitting parameters summarized in Table 4. The fits yielded $\chi^2\_reduced$ values of 222 for $Cu_{0.1}/NC$ and 498 for $Cu_{0.2}/NC$, indicating satisfactory agreement. For $Cu_{0.1}/NC$, fitting using a Feff8-generated Cu−N scattering path at 1.93 Å supports the presence of isolated Cu^{II} centers in a planar, porphyrin-like geometry, with a coordination number (CN) of 3.6 ± 0.4. The slightly shortened Cu−N bond length relative to typical values (~1.95 Å), along with the XANES feature at 8977.0 eV, suggests a mixture of Cu^{II} and Cu^I species. The sub-4 coordination number points out a minor contribution from Cu^I in a distorted trigonal or tetrahedral environment.

For $Cu_{0.2}/NC$, a combination of Cu−N (1.95 Å) and Cu−Cu paths (2.55 and 3.61 Å) is required to achieve a reliable fit. The corresponding coordination numbers are 2.3 ± 0.7 for Cu−N, 5.0 ± 0.7 for short-range Cu−Cu, and 2.5 ± 0.7 for longer-range Cu−Cu interactions. The former coordination number can be explained by the presence of trigonal Cu^I species combined with planar Cu^{II} species. These features, together with the XANES transitions at 8976.0 and 8977.0 eV, confirm the coexistence of metallic Cu^0 and Cu^I species. The reduced Cu−Cu coordination number relative to bulk Cu (CN = 12) is consistent with the presence of ultrasmall Cu clusters (<2 nm), as observed by AC-HAADF-STEM.

3.3. Catalytic Performance. The catalytic performance of Cu_x/NC catalysts in methanol oxidative carbonylation is
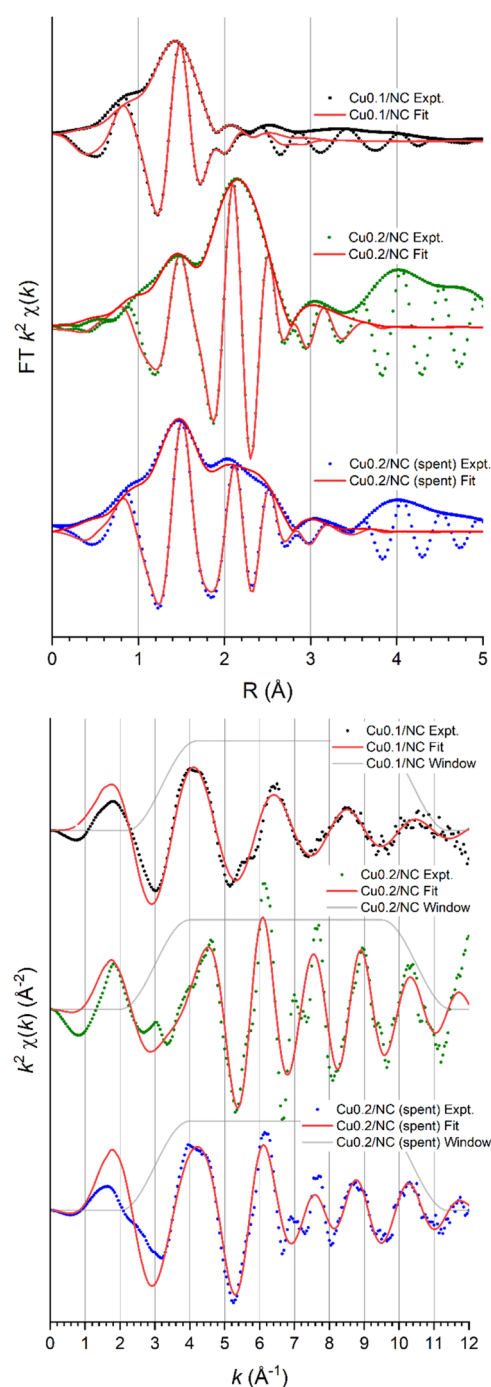
Figure 6. Experimental and fitted EXAFS plots for samples $Cu_{0.1}/NC$, $Cu_{0.2}/NC$ and $Cu_{0.2}/NC\_spent$.

summarized in Table 5. A control experiment using $Cu_{0.0}/NC$ reveals no activity, confirming the essential catalytic role of Cu. Among the tested catalysts, $Cu_{0.2}/NC$ exhibits the highest space-time yield for dimethyl carbonate at 3249 mg·g^{-1}·h^{-1} ($TOF_{DMC,B}$ = 34 h^{-1}), with a methanol conversion of 5.86% and a near-quantitative selectivity to DMC (99.41%). $Cu_{0.2}/NC$ also exhibits the highest $TOF_{DMC,S}$ with a value of 294 h^{-1}, indicating optimal utilization of active sites.

Unlike $Cu_{0.2}/NC$, the comparatively lower space-time yield of DMC formation for $Cu_{0.1}/NC$ is attributed to the lower Cu loading, while the reduced performance of $Cu_{0.3}/NC$ and $Cu_{0.4}/NC$ is ascribed to decreased Cu dispersion due to

Table 4. Results of EXAFS Fittings

	shell	N	R (Å)	σ^2 (10^{-3} Å^2)	ΔE_0 (eV)	$\chi_{reduced}^2$
Cu$_{0.1}$/NC	Cu−N	3.6 ± 0.4	1.92 ± 0.01	6.2 ± 2	−7 ± 2	222
Cu$_{0.2}$/NC	Cu−Cu1	5.0 ± 0.7	2.55 ± 0.01	8.5 ± 1	−5.2 ± 2	498
	Cu−Cu2	2.5 ± 0.7	3.61 ± 0.01	13.6 ± 4		
	Cu−N	2.3 ± 0.7	1.95 ± 0.02	9.4 ± 5		
Cu$_{0.2}$/NC_spent	Cu−Cu1	2.3 ± 0.7	2.56 ± 0.008	7.9 ± 2	−5.1 ± 2	457
	Cu−Cu2	1.2 ± 0.7	3.66 ± 0.09	14.9 ± 13		
	Cu−N	3.4 ± 0.5	1.96 ± 0.007	5.8 ± 2		

Table 5. Catalytic Performance of Cu$_x$/NC Catalysts in the Oxidative Carbonylation of Methanol[a]

catalyst	C_{MeOH} (%)	S_{DMC} (%)	S_{MF} (%)	S_{DMM} (%)	STY$_{DMC}$ (mg·g^{-1}·h^{-1})	TOF$_{DMC,B}$ (h^{-1})	TOF$_{DMC,S}$ (h^{-1})
NC	0	0	0	0	0	0	0
Cu$_{0.1}$/NC	2.65	98.50	1.40	0.10	1312	31	122
Cu$_{0.2}$/NC	5.86	99.41	0.42	0.17	3249	34	294
Cu$_{0.3}$/NC	4.64	97.85	1.81	0.34	2534	20	56
Cu$_{0.4}$/NC	3.62	98.17	1.47	0.36	1957	11	48

[a]Reaction conditions: methanol (10 mL), CO (3.6 MPa), O$_2$ (0.4 MPa), catalyst (0.1 g), stirring rate (300 rpm), reaction at 120 °C for 2h.

Table 6. Comparison of Catalytic Performance over Cu$_{0.2}$/NC and Recently Reported Catalysts[a]

catalyst	Cu loading (wt %)	Cu speciation particle size (nm)	surface Cu^{2+} (%)	C_{MeOH} (%)	S_{DMC} (%)	STY$_{DMC}$ (mg·g^{-1}·h^{-1})	TOF$_{DMC,B}$ (h^{-1})	TOF$_{DMC,S}$ (h^{-1})	number of runs (n)	deactivation after the nth run (%)[e]	refs
Cu$_{0.2}$/NC	**6.7**	**Atoms, clusters (<0.8 nm)**	**59.5**	**5.9**	**99.4**	**3249**	**34.4**	**294**	**7**	**5.8 ± 4.0**	**This work**
Cu/NCNS-8	10.6	11 nm/clusters (0.91 nm)[b]	0	9.6	90.5	3227	23.7	55	10	11−37	34
Cu/SAC	0.05	2.2−5.2	44.8	9.4	90.9	316	13.2	65	5	10.4	76
Cu/NC-60-H	9.1	6.5	28.8	7.7	94.4	1365	10.6	74	6	38.5	77
Cu/NG-10	7.0	7.5−29.1		3.1	97.6	1665	16.8		5	12.0	32
Cu/NCNT200	8.0	2.6−10.5	53.3	2.4	97.8	1790	15.8	255	4	12.9	31
Cu/MMC-3	11.4	3.3−10.6	10.9	7.2	95.1	3900	24.1	89[d]	4	20.5	28
Cu@NG/C-700	8.6	15[c]	24.4	2.8	92.3	1881	15.4	109			23
Cu/CNT(2−5)	8.0	3.0−4.9	55.5	4.2	91.2	2200	21.9	289	6	40.9	26
Cu@HCS-5		5.5−8.1		3.7	90.4	2504			5	50.2	22

[a]Range of operation conditions: temperature (110−120 °C), reaction time (1.5−2 h), methanol (5−30 mL), CO (2.0−3.6 MPa), O$_2$ (0.4−1.0 MPa), catalyst (0.1−1.0 g), stirring rate (300 rpm). [b]The initial Cu nanoparticles evolved into Cu clusters after the 2nd catalytic run by Cu reconstruction. [c]Cu nanoparticles were encapsulated. [d]Based on surface Cu$^+$. [e]Measured using eq 13 with error estimated using eq 14.

nanoparticle formation, along with increased activation energy barriers for CO insertion.[41] All catalysts exhibit high DMC selectivity (>97%), which is consistent with the absence of acidic sites that could promote side reactions.

Reduction pretreatment of Cu$_{0.2}$/NC at 400 °C for 2 h (heating rates: 1 and 5 °C·min^{-1}) exerts no significant effect on either Cu dispersion (Figure S12) or catalytic activity, with methanol conversions of 5.9% and 6.0%, respectively. These results confirm the structural and catalytic robustness of Cu$_{0.2}$/ NC under reductive conditions.

When benchmarked against literature-reported Cu-based catalysts for methanol oxidative carbonylation (Table 6), Cu$_{0.2}$/NC demonstrates the highest space-time yields and TOF values, highlighting its superior catalytic efficiency.

To optimize the reaction conditions, the effect of Cu$_{0.2}$/NC weight, reaction temperature, and reaction time on the catalytic performance was systematically investigated (Figure S13). Methanol conversion increased sharply with catalyst weight up to 0.1 g (Figure S13a), beyond which it plateaued, indicating a shift from kinetic to mass-transfer-limited regime. The reaction can be thermally activated at temperatures above

120 °C (Figure S13b). At 120 °C, methanol conversion stabilized after 1.5 h with DMC selectivity consistently exceeding 97% (Figure S13c), confirming the suitability of these conditions for efficient DMC production.

Under the optimized conditions, Cu$_{0.2}$/NC was selected for long-term stability testing over seven consecutive catalytic runs (Figure. 7 and Table S1). After each run, the catalyst was recovered by filtration, vacuum-dried at 60 °C for 2 h, and reused. The methanol conversion and DMC selectivity keep virtually unchanged over all runs, with negligible deactivation within experimental error after 7 runs. These results demonstrate the high stability and reusability of Cu$_{0.2}$/NC, surpassing the performance of previously reported Cu-based catalysts (Table 6). To our knowledge, Cu$_{0.2}$/NC exhibits the highest stability reported to date for the methanol oxidative carbonylation reaction, while maintaining outstanding space-time yield and TOF$_{DMC,S}$.

3.4. Characterization of Cu$_{0.2}$/NC_spent. Deactivation of Cu-based catalysts typically arises from leaching, agglomeration, or overoxidation of the active Cu species. To assess the structural and chemical integrity of Cu$_{0.2}$/NC after prolonged
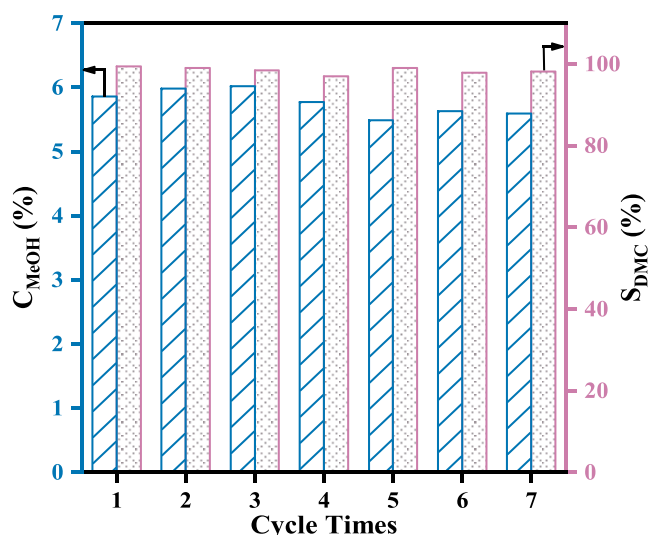
Figure 7. Catalytic performance of $Cu_{0.2}/NC$ in seven consecutive runs. Reaction conditions: methanol (10 mL), CO (3.6 MPa), O_2 (0.4 MPa), catalyst (0.1 g), stirring rate (300 rpm), reaction at 120 °C for 2 h. The catalyst was vacuum-dried at 60 °C for 2 h after each run. The error was <3% in all measurements.

catalytic use, the spent catalyst ($Cu_{0.2}/NC\_spent$) recovered after the seventh run was analyzed by ICP-OES, TEM, N_2 adsorption–desorption at −196 °C, and XPS (Table S2). In addition, leaching tests were performed after each run to quantify the Cu content in the liquid phase.

The Cu content of $Cu_{0.2}/NC$ decreases only slightly from 6.73 wt % (fresh) to 6.58 wt % (after 7 runs), while the Cu concentration in the reaction solution remains extremely

low—1.44 ppm after the first run and 4.28 ppm after the seventh run—indicating that Cu leaching is minimal and does not significantly contribute to catalyst deactivation. Furthermore, N_2 physisorption analysis revealed that the isotherm profile and textural properties of the spent catalyst (Figure 8d) are nearly identical to those of the fresh sample, retaining a high specific surface area of 1197 $m^2 \cdot g^{-1}$. This confirms that the pore structure and surface area of $Cu_{0.2}/NC$ remain intact after repeated catalytic runs.

TEM micrographs (Figure 8a,b) clearly demonstrate that the $Cu_{0.2}/NC\_spent$ retains its initial octahedral particle morphology with no evidence of agglomeration or nanoparticle formation, indicating that atomic and cluster-like Cu species remain well-dispersed after the reaction. Elemental mapping of Cu and the SAED pattern (Figure 8c) further confirm a homogeneous distribution of Cu across the carbon nitride matrix and the absence of crystalline Cu nanoparticles.

XPS analysis of the Cu $2p_{3/2}$ region (Figure 8e) reveals three distinct peaks at binding energies of 934.7, 934.0, and 932.3 eV, corresponding to surface $Cu(OH)_2$, CuO, and mixed Cu^0/Cu^+ species, respectively. The surface molar fraction of Cu^0/Cu^+ is 35.5%, only slightly lower than that of the fresh catalyst (40.5%), indicating minimal surface oxidation or structural change upon reuse.

The derivative plot of the XANES spectrum of $Cu_{0.2}/NC\_spent$ shows the same features as the parent $Cu_{0.2}/NC$ (Figure 5). Feature (A) appearing at 8977.0 eV is clearly visible belonging to Cu^{II} species. Features (B) and (D) can also be observed at 8979.0 and 8984.2 eV, respectively, that can be ascribed to Cu^0 species. Additionally, a new feature labeled (E) at 8987.2 eV, that is only present in sample $Cu_{0.2}/$
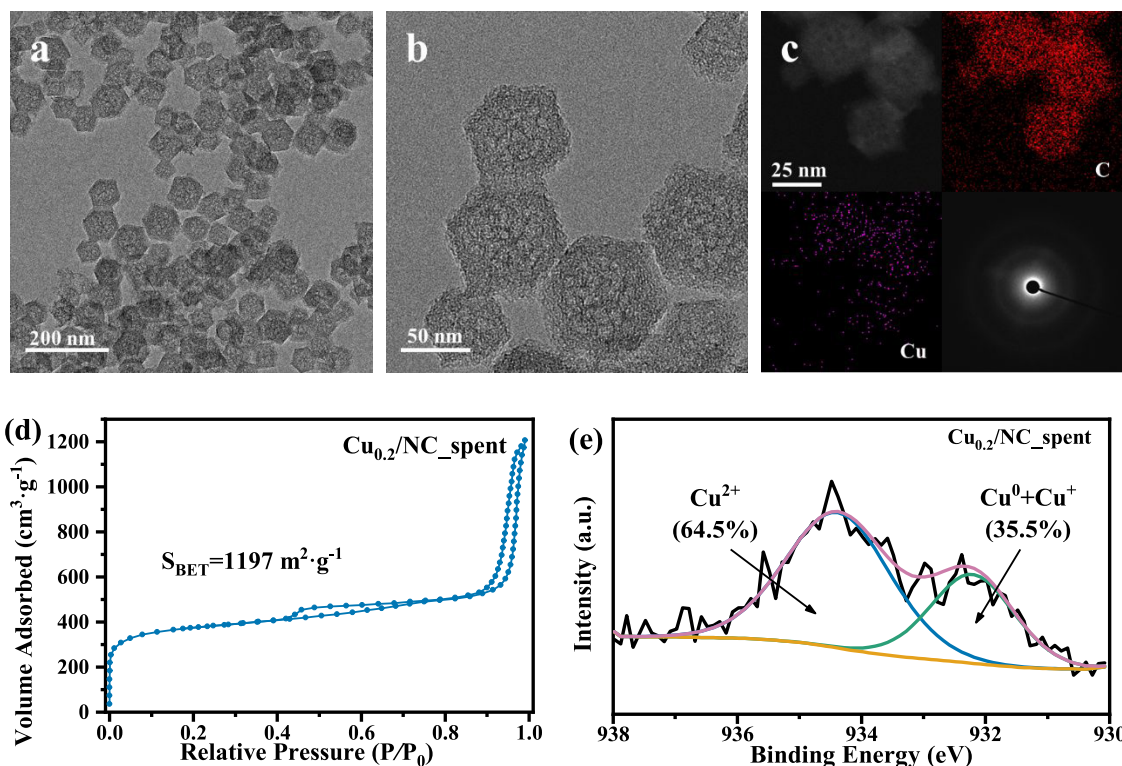
Figure 8. (a, b) TEM micrographs, (c) TEM-EDS elemental mapping and SAED pattern, (d) N_2 adsorption–desorption isotherms at −196 °C and (e) Cu $2p_{3/2}$ XPS spectra of $Cu_{0.2}/NC\_spent$ after reaction at 7th.

NC_spent, has been observed in systems with 5/6 coordination in planar Cu^{II} systems.[78,79]

EXAFS fitting (χ^2_reduced = 457) of $Cu_{0.2}$/NC_spent (Figure 6) reveals the persistence of a Cu–N coordination shell (1.96 Å) and a Cu−Cu shell with two components (2.56 and 3.66 Å), indicating retention of the metallic Cu^0 component postreaction. The fitted Cu−N coordination number increases to 3.4 ± 0.7, consistent with the formation of an out-of-plane 5-/6-coordinate Cu^{II} species. The Cu−Cu coordination numbers for Cu^I and Cu^0 species are 2.3 ± 0.7 and 1.2 ± 0.7, respectively, slightly lower than in the fresh sample, suggesting a decrease in cluster size upon recycling.

4. CONCLUSIONS

In summary, a reproducible, robust Cu catalyst supported over carbon nitride was prepared by pyrolysis of a Cu-doped ZIF-8 precursor and implemented for methanol oxidative carbonylation to dimethyl carbonate. Cu^I and Cu^{II} species were highly dispersed in the form of single atoms and ultrasmall Cu^0 clusters (size <0.60 nm) on the surface of carbon nitride at high Cu loadings (up to 6.5 wt %) as confirmed by XAS, XPS, HR-TEM, and HAADF-STEM, whereas Cu_2O and Cu^0 nanoparticles were encapsulated within the carbon matrix as revealed by XRD. Increasing Cu loading led to more extensive nanoparticle formation, likely due to decreased Zn-induced spatial constraints.

XAS provides direct evidence of Cu speciation on $Cu_{0.1}$/NC and $Cu_{0.2}$/NC. For $Cu_{0.1}$/NC, fitting of EXAFS spectra supports the presence of isolated Cu^{II} and Cu^I centers in a planar, porphyrin-like geometry, with a coordination number (CN) of 3.6 ± 0.4. For $Cu_{0.2}$/NC, a combination of Cu−N (1.95 Å) and Cu−Cu paths (2.55 and 3.61 Å) is required to achieve a reliable fit. The corresponding coordination numbers are 2.3 ± 0.7 for Cu−N, 5.0 ± 0.7 for short-range Cu−Cu, and 2.5 ± 0.7 for longer-range Cu−Cu interactions. The former coordination number is consistent with trigonal Cu^I species combined with planar Cu^{II} species. The low Cu−Cu coordination numbers relative to bulk Cu are consistent with the presence of ultrasmall Cu clusters (<2 nm), as observed by AC-HAADF-STEM.

Among the catalyst series, $Cu_{0.2}$/NC exhibited optimal performance in the oxidative carbonylation of methanol to dimethyl carbonate (DMC), achieving a selectivity of 99.4%, a space-time yield (STY_{DMC}) of 3249 mg·g^{-1}·h^{-1}, and turnover frequencies of 34.4 h^{-1} (based on bulk Cu) and 294 h^{-1} (based on surface Cu). The outstanding activity is attributed to the high dispersion of Cu^0 and Cu^+ species and the absence of acid sites, which suppress side reactions.

The atomic and cluster-like Cu architecture imparted exceptional stability. $Cu_{0.2}$/NC maintained its catalytic performance over seven consecutive runs, with negligible loss in activity or selectivity. Structural analysis postreaction confirmed the preservation of Cu speciation, and architecture with a decrease in Cu cluster size upon recycling indicating minimal deactivation due to leaching, sintering, or oxidation. This level of stability and performance exceeds that of previously reported Cu-based catalysts for this reaction, highlighting the importance of precise control over Cu atom distribution and Cu-support interactions.

■ ASSOCIATED CONTENT

ⓈＩ Supporting Information

The Supporting Information is available free of charge at https://pubs.acs.org/doi/10.1021/acssuschemeng.5c04760.

SEM and TEM images of Cu_x-ZIF-8 precursors and Cu_x/NC catalysts, N_2 adsorption−desorption isotherms at −196 °C and BJH pore size distributions of Cu_x-ZIF-8 precursors, NH_3-TPD profiles and H_2-TPR profiles of Cu_x/NC catalysts, STEM-EDS elemental mapping of $Cu_{0.1}$/NC, $Cu_{0.2}$/NC, $Cu_{0.3}$/NC and $Cu_{0.4}$/NC, SAED patterns of $Cu_{0.1}$/NC, $Cu_{0.3}$/NC and $Cu_{0.4}$/NC, XPS spectra of Cu_x/NC catalysts, catalytic performance of Cu_x/NC catalysts as a function of the catalyst weight, temperature and reaction time, bulk composition and textural properties of Cu_x-ZIF-8 precursors, catalytic performance of $Cu_{0.2}$/NC in seven consecutive runs (PDF)

■ AUTHOR INFORMATION

Corresponding Authors

Shanlin Gao − *Shanghai Engineering Research Center of Coal-Based Polygeneration, Shanghai Huayi Holding Group Co., Ltd, Shanghai 200040, China*; Email: gaoshanlin@shhuayi.com

Marc Pera-Titus − *Cardiff Catalysis Institute, School of Chemistry, Cardiff University, Cardiff CF10 3AT, U.K.*; ⓞ orcid.org/0000-0001-7335-1424; Email: peratitusm@cardiff.ac.uk

Zhiyong Deng − *College of Resources and Environment, Chengdu University of Information Technology (CUIT), Chengdu 610225, China; Air Environmental Modeling and Pollution Controlling Key Laboratory of Sichuan Higher Education Institutes, Chengdu 610225, China*; Email: dengzhiyong@cuit.edu.cn

Authors

Wenjie Li − *College of Resources and Environment, Chengdu University of Information Technology (CUIT), Chengdu 610225, China*

Chunbo Lai − *Shanghai Engineering Research Center of Coal-Based Polygeneration, Shanghai Huayi Holding Group Co., Ltd, Shanghai 200040, China*

Xinling Li − *College of Resources and Environment, Chengdu University of Information Technology (CUIT), Chengdu 610225, China*

Wanjing Xiao − *College of Resources and Environment, Chengdu University of Information Technology (CUIT), Chengdu 610225, China*

Xinyu Wang − *College of Resources and Environment, Chengdu University of Information Technology (CUIT), Chengdu 610225, China*

Huibo Lin − *College of Resources and Environment, Chengdu University of Information Technology (CUIT), Chengdu 610225, China*

Yang Zhang − *College of Resources and Environment, Chengdu University of Information Technology (CUIT), Chengdu 610225, China*

Haijun Liu − *College of Resources and Environment, Chengdu University of Information Technology (CUIT), Chengdu 610225, China*

Gan Yang − *College of Resources and Environment, Chengdu University of Information Technology (CUIT), Chengdu 610225, China*

Chenghua Xu − *College of Resources and Environment, Chengdu University of Information Technology (CUIT), Chengdu 610225, China; Air Environmental Modeling and Pollution Controlling Key Laboratory of Sichuan Higher Education Institutes, Chengdu 610225, China*

Luke J. R. Higgins − *Research Complex at Harwell, Rutherford Appleton Laboratories, Didcot OX11 0FA, U.K.; Diamond Light Source, Rutherford Appleton Laboratories, Didcot OX11 0FA, U.K.*

Andrew M. Beale − *Research Complex at Harwell, Rutherford Appleton Laboratories, Didcot OX11 0FA, U.K.; Department of Chemistry, University College London, London WC1H 0AJ, U.K.;* ⊙ orcid.org/0000-0002-0923-1433

Complete contact information is available at:
https://pubs.acs.org/10.1021/acssuschemeng.5c04760

Author Contributions

W.L.: Conceptualization, methodology, data curation, investigation, writing original draft. S.G.: Review and editing, funding acquisition. C.L.: Review and editing. X.L.: Review and editing. W.X.: Review and editing. X.W.: Review and editing. H.L.: Review and editing. Y.Z.: Review and editing. H.L.: Review and editing. G.Y.: Review and editing. C.X.: Review and editing. L.J.R.H.: Investigation, methodology, writing original draft. A.M.B.: Methodology, writing original draft. M.P.-T.: Conceptualization, methodology, review and editing. Z.D.: Conceptualization, methodology, review and editing, funding acquisition.

Notes

The authors declare no competing financial interest.

■ REFERENCES

(1) Selva, M.; Perosa, A.; Rodríguez-Padrón, D.; Luque, R. Applications of dimethyl carbonate for the chemical upgrading of biosourced platform chemicals. *ACS Sustainable Chem. Eng.* **2019**, *7*, 6471−6479.

(2) Fiorani, G.; Perosa, A.; Selva, M. Dimethyl carbonate: A versatile reagent for a sustainable valorization of renewables. *Green Chem.* **2018**, *20*, 288−322.

(3) Zhang, M.; Xu, Y. H.; Williams, B. L.; Xiao, M.; Wang, S. J.; Han, D. M.; Sun, L. Y.; Meng, Y. Z. Catalytic materials for direct synthesis of dimethyl carbonate (DMC) from CO_2. *J. Cleaner Prod.* **2021**, *279*, No. 123344.

(4) Tan, H. Z.; Wang, Z. Q.; Xu, Z. N.; Sun, J.; Xu, Y. P.; Chen, Q. S.; Chen, Y. M.; Guo, G. C. Review on the synthesis of dimethyl carbonate. *Catal. Today* **2018**, *316*, 2−12.

(5) Huang, S. Y.; Yan, B.; Wang, S. P.; Ma, X. B. Recent advances in dialkyl carbonates synthesis and applications. *Chem. Soc. Rev.* **2015**, *44*, 3079−3116.

(6) Kumar, P.; Srivastava, V. C.; Štangar, U. L.; Mušič, B.; Mishra, I. M.; Meng, Y. Recent progress in dimethyl carbonate synthesis using different feedstock and techniques in the presence of heterogeneous catalysts. *Catal. Rev.* **2021**, *63*, 363−421.

(7) Hallgren, J. E.; Lucas, G. M. Carbonylation of Alkanols. U.S. Patent US4360477, 1981.

(8) Garcia-Herrero, I.; Cuellar-France, R. M.; Enriquez-Gutierrez, V. M.; Alvarez-Guerra, M.; Irabien, A.; Azapagic, A. Environmental assessment of dimethyl carbonate production: comparison of a novel electrosynthesis route utilizing CO_2 with a commercial oxidative carbonylation process. *ACS Sustainable Chem. Eng.* **2016**, *4*, 2088−2097.

(9) Sato, Y.; Kagotani, M.; Souma, Y. A new type of support 'bipyridine containing aromatic polyamide' to $CuCl_2$ for synthesis of dimethyl carbonate (DMC) by oxidative carbonylation of methanol. *J. Mol. Catal. A: Chem.* **2000**, *151*, 79−85.

(10) Wang, R. Y.; Li, Z.; Zheng, H. Y.; Xie, K. C. Preparation of Chlorine-Free Cu/AC Catalyst and Its Catalytic Properties for Vapor Phase Oxidative Carbonylation of Methanol. *Chin. J. Catal.* **2010**, *31*, 851−856.

(11) Itoh, H.; Watanabe, Y.; Mori, K.; Umino, H. Synthesis of dimethyl carbonate by vapor phase oxidative carbonylation of methanol. *Green Chem.* **2003**, *5*, 558−562.

(12) Mo, W. L.; Xiong, H.; Li, T.; Guo, X. C.; Li, G. X. The catalytic performance and corrosion inhibition of CuCl/Schiff base system in homogeneous oxidative carbonylation of methanol. *J. Mol. Catal. A: Chem.* **2006**, *247*, 227−232.

(13) Drake, I. J.; Zhang, Y. H.; Briggs, D.; Lim, B.; Chau, T.; Bell, A. T. The local environment of Cu^+ in Cu-Y zeolite and its relationship to the synthesis of dimethyl carbonate. *J. Phys. Chem. B* **2006**, *110*, 11654−11664.

(14) Zhang, Y. H.; Briggs, D. N.; de Smit, E.; Bell, A. T. Effects of zeolite structure and composition on the synthesis of dimethyl carbonate by oxidative carbonylation of methanol on Cu-exchanged Y, ZSM-5, and Mordenite. *J. Catal.* **2007**, *251*, 443−452.

(15) Li, Y. J.; Yan, L. F.; Zheng, H. Y.; Li, Z. Effects of acid treatment on pore structure and oxidation carbonylation performance of CuY catalysts. *Chin. J. Inorg. Chem.* **2015**, *31*, 2315−2323.

(16) Yan, L. F.; Zhang, G. Q.; Li, Y. J.; Zheng, H. Y.; Li, Z. Influence of mesoporous modulation on CuY catalyst for oxidative carbonylation of methanol. *Chin. J. Inorg. Chem.* **2017**, *33*, 1435−1442.

(17) Zhou, H. X.; Wang, S. P.; Wang, B. W.; Ma, X. B.; Huang, S. Y. Oxycarbonylation of methanol over modified CuY: Enhanced activity by improving accessibility of active sites. *Chin. Chem. Lett.* **2019**, *30*, 775−778.

(18) Anderson, S. A.; Manthata, S.; Root, T. W. The decomposition of dimethyl carbonate over copper zeolite catalysts. *Appl. Catal., A* **2005**, *280*, 117−124.

(19) Sun, R. Y.; Delidovich, I.; Palkovits, R. Dimethoxymethane as a cleaner synthetic fuel: Synthetic methods, catalysts, and reaction mechanism. *ACS Catal.* **2019**, *9*, 1298−1318.

(20) Zhao, P. Y.; Yan, J. F.; Shan, B. Q.; Zhang, Y.; Zhao, Z. Y.; Liu, L.; Su, Z.; Cheng, W.; Xu, X. M. Copper nanoparticles control of carbon supported copper catalysts for dimethyl carbonate synthesis: A short review. *Mol. Catal.* **2023**, *536*, No. 112910.

(21) Zhang, G. Q.; Li, Z.; Zheng, H. Y.; Fu, T. J.; Ju, Y. B.; Wang, Y. C. Influence of the surface oxygenated groups of activated carbon on preparation of a nano Cu/AC catalyst and heterogeneous catalysis in the oxidative carbonylation of methanol. *Appl. Catal., B* **2015**, *179*, 95−105.

(22) Shi, R. N.; Wang, J.; Zhao, J. X.; Liu, S. S.; Hao, P. P.; Li, Z.; Ren, J. Cu nanoparticles encapsulated with hollow carbon spheres for methanol oxidative carbonylation: Tuning of the catalytic properties by particle size control. *Appl. Surf. Sci.* **2018**, *459*, 707−715.

(23) Shi, R. N.; Zhao, J. X.; Quan, Y.; Pei, Y. L.; Wang, X. H.; Li, Z.; Ren, J. Carbon-supported nitrogen-doped graphene-wrapped copper nanoparticles: An effective catalyst for the oxidative carbonylation of methanol. *Ind. Eng. Chem. Res.* **2021**, *60*, 2944−2953.

(24) Ren, J.; Hao, P. P.; Sun, W.; Shi, R. N.; Liu, S. S. Ordered mesoporous silica-carbon-supported copper catalyst as an efficient

and stable catalyst for catalytic oxidative carbonylation. *Chem. Eng. J.* **2017**, *328*, 673−682.

(25) Zhang, G. Q.; Yan, J. F.; Wang, J. J.; Jia, D. S.; Zheng, H. Y.; Li, Z. Effect of carbon support on the catalytic performance of Cu-based nanoparticles for oxidative carbonylation of methanol. *Appl. Surf. Sci.* **2018**, *455*, 696−704.

(26) Zhao, D.; Zhang, G. Q.; Yan, L. F.; Kong, L. Q.; Zheng, H. Y.; Mi, J.; Li, Z. Carbon nanotube-supported Cu-based catalysts for oxidative carbonylation of methanol to methyl carbonate: Effect of nanotube pore size. *Catal. Sci. Technol.* **2020**, *10*, 2615−2626.

(27) Wang, J. J.; Yang, L. F.; Fu, T. J.; Meng, F. H.; Li, Z. The confinement effects of ordered mesoporous carbon on copper nanoparticles for methanol oxidative carbonylation. *New J. Chem.* **2022**, *46*, 2980−2988.

(28) Wang, J. J.; Fu, T. J.; Meng, F.; Zhao, D.; Chuang, S. S. C.; Li, Z. Highly active catalysis of methanol oxidative carbonylation over nano Cu$_2$O supported on micropore-rich mesoporous carbon. *Appl. Catal., B* **2022**, *303*, No. 120890.

(29) Pei, Y. L.; Zhao, J. X.; Shi, R. N.; Wang, X. H.; Li, Z.; Ren, J. Hierarchical porous carbon-supported copper nanoparticles as an efficient catalyst for the dimethyl carbonate synthesis. *Catal. Lett.* **2019**, *149*, 3184−3193.

(30) Li, H. X.; Zhao, J. X.; Shi, R. N.; Hao, P. P.; Liu, S. S.; Li, Z.; Ren, J. Remarkable activity of nitrogen-doped hollow carbon spheres encapsulated Cu on synthesis of dimethyl carbonate: Role of effective nitrogen. *Appl. Surf. Sci.* **2018**, *436*, 803−813.

(31) Zhang, G. Q.; Zhao, D.; Yan, J. F.; Jia, D. S.; Zheng, H. Y.; Mi, J.; Li, Z. The promotion and stabilization effects of surface nitrogen containing groups of CNT on Cu-based nanoparticles in the oxidative carbonylation reaction. *Appl. Catal., A* **2019**, *579*, 18−29.

(32) Shi, R. N.; Zhao, J. X.; Liu, S. S.; Sun, W.; Li, H. X.; Hao, P. P.; Li, Z.; Ren, J. Nitrogen-doped graphene supported copper catalysts for methanol oxidative carbonylation: Enhancement of catalytic activity and stability by nitrogen species. *Carbon* **2018**, *130*, 185−195.

(33) Wang, G.; Cao, M.; Bai, Y.; Wang, Q.; Zeng, Y. Catalyst for Oxidative Carbonylation of Methanol to Synthesize Dimethyl Carbonate and Preparation Method and Applications Thereof. U.S. Patent US2023/0321641A1, 2022.

(34) Pei, Y. L.; Quan, Y. H.; Wang, X. H.; Zhao, J. X.; Shi, R. N.; Li, Z.; Ren, J. Surface reconstruction induced highly efficient N-doped carbon nanosheet supported copper cluster catalysts for dimethyl carbonate synthesis. *Appl. Catal., B* **2022**, *300*, No. 120718.

(35) Zhang, Y. H.; Bell, A. T. The mechanism of dimethyl carbonate synthesis on Cu-exchanged zeolite Y. *J. Catal.* **2008**, *255*, 153−161.

(36) Ren, X. J.; Quan, Y. H.; Yang, W.; Zhao, J. X.; Shi, R. N.; Ren, J. Highly efficient super activated carbon supported ultra-low loading copper catalyst for the oxidative carbonylation of methanol to dimethyl carbonate. *Mol. Catal.* **2022**, *531*, No. 112694.

(37) Ren, J.; Wang, W.; Wang, D. L.; Zuo, Z. J.; Lin, J. Y.; Li, Z. A theoretical investigation on the mechanism of dimethyl carbonate formation on Cu/AC catalyst. *Appl. Catal., A* **2014**, *472*, 47−52.

(38) Sun, W.; Shi, R. N.; Wang, X. H.; Liu, S. S.; Han, X. X.; Zhao, C. F.; Li, Z.; Ren, J. Density-functional theory study of dimethyl carbonate synthesis by methanol oxidative carbonylation on single-atom Cu$_1$/graphene catalyst. *Appl. Surf. Sci.* **2017**, *425*, 291−300.

(39) Kang, L.; Zhang, J.; Zhang, R. G.; Ling, L. X.; Wang, B. J. Insight into the formation mechanism and kinetics for the oxidative carbonylation of methanol to dimethyl carbonate over CuO catalyst: Effects of Cu valence state and solvent environment. *Mol. Catal.* **2018**, *449*, 38−48.

(40) Zheng, H. Y.; Qin, Y.; Li, Z.; Zhang, G. Q.; Meng, F. H. Copper states in Cu/AC Catalyst during gas-phase oxidative carbonylation of methanol to dimethyl carbonate. *Chin. J. Inorg. Chem.* **2014**, *30*, 2111−2118.

(41) Wang, J.; Shi, R. N.; Hao, P. P.; Sun, W.; Liu, S. S.; Li, Z.; Ren, J. Influence of oxygen-containing groups of activated carbon aerogels on copper/activated carbon aerogels catalyst and synthesis of dimethyl carbonate. *J. Mater. Sci.* **2018**, *53*, 1833−1850.

(42) Konnerth, H.; Matsagar, B. M.; Chen, S. S.; Prechtl, M. H. G.; Shieh, F.-K.; Wu, K. C. W. Metal-organic framework (MOF)-derived catalysts for fine chemical production. *Coord. Chem. Rev.* **2020**, *416*, No. 213319.

(43) Cheng, N. Y.; Ren, L.; Casillas, G.; Zhou, S.; Zhuang, J. C.; Wang, L.; Xu, X.; Dou, S. X.; Du, Y. Rational design of two-dimensional hybrid Co/N-doped carbon nanosheet arrays for efficient bi-functional electrocatalysis. *Sustainable Energy Fuels* **2019**, *3*, 1757−1763.

(44) Yin, P. Q.; Yao, T.; Wu, Y.; Zheng, L. R.; Lin, Y.; Liu, W.; Ju, H. X.; Zhu, J.; Hong, X.; Deng, Z. X.; Zhou, G.; Wei, S. Q.; Li, Y. D. Single cobalt atoms with precise N-coordination as superior oxygen reduction reaction catalysts. *Angew. Chem., Int. Ed.* **2016**, *55*, 10800−10805.

(45) Li, G. R.; Zhang, H. F.; Yu, X. T.; Lei, Z. P.; Yin, F. X.; He, X. B. Highly efficient Co/NC catalyst derived from ZIF-67 for hydrogen generation through ammonia decomposition. *Int. J. Hydrogen Energy* **2022**, *47*, 12882−12892.

(46) Ma, S. Y.; Han, W. G.; Han, W. L.; Dong, F.; Tang, Z. C. Recent advances and future perspectives in MOF-derived single-atom catalysts and their application: A review. *J. Mater. Chem. A* **2023**, *11*, 3315−3363.

(47) Sun, T. T.; Xu, L. B.; Wang, D. S.; Li, Y. D. Metal organic frameworks derived single atom catalysts for electrocatalytic energy conversion. *Nano Res.* **2019**, *12*, 2067−2080.

(48) Lee, H.; Kwon, C.; Vikneshvaran, S.; Lee, S.; Lee, S.-Y. Partial oxidation of methane to methyl oxygenates with enhanced selectivity using a single-atom copper catalyst on amorphous carbon support. *Appl. Surf. Sci.* **2023**, *639*, No. 158289.

(49) Schejn, A.; Aboulaich, A.; Balan, L.; Falk, V.; Lalevée, J.; Medjahdi, G.; Aranda, L.; Mozet, K.; Schneider, R. Cu^{2+}-doped zeolitic imidazolate frameworks (ZIF-8): Efficient and stable catalysts for cycloadditions and condensation reactions. *Catal. Sci. Technol.* **2015**, *5*, 1829−1839.

(50) Perez, O. L.; Romeu, D.; Yacaman, M. J. The relation between dispersion and particle size on supported catalysts. *J. Catal.* **1983**, *79*, 240−241.

(51) Bergeret, G.; Gallezot, P. Particle Size and Dispersion Measurements. In *Handbook of Heterogeneous Catalysis*; Ertl, G.; Knozinger, H.; Weitkamp, J., Eds.; Wiley-VCH: Weinheim, 1997; pp 439−491.

(52) Wang, Q. T.; Cheng, S. N.; Ren, S. F.; Zheng, Z. X. Construction of molecularly imprinted voltammetric sensor based on Cu-N-C polyhedron porous carbon from Cu doping ZIF-8 for the selective determination of norfloxacin. *Microchem. J.* **2022**, *183*, No. 107963.

(53) Ahmad, A.; Iqbal, N.; Noor, T.; Hassan, A.; Khan, U. A.; Wahab, A.; Raza, M. A.; Ashraf, S. Cu-doped zeolite imidazole framework (ZIF-8) for effective electrocatalytic CO$_2$ reduction. *J. CO$_2$ Util.* **2021**, *48*, No. 110523.

(54) Awadallah-F, A.; Hillman, F.; Al-Muhtaseb, S. A.; Jeong, H.-K. On the nanogate-opening pressures of copper-doped zeolitic imidazolate framework ZIF-8 for the adsorption of propane, propylene, isobutane, and n-butane. *J. Mater. Sci.* **2019**, *54*, 5513−5527.

(55) Goyal, S.; Shaharun, M. S.; Kait, C. F.; Abdullah, B. Effect of monometallic copper on zeolitic imidazolate framework-8 synthesized by hydrothermal method. *J. Phys. Conf. Ser.* **2018**, *1123*, No. 012062.

(56) Nagarjun, N.; Dhakshinamoorthy, A. A Cu-doped ZIF-8 metal organic framework as a heterogeneous solid catalyst for aerobic oxidation of benzylic hydrocarbons. *New J. Chem.* **2019**, *43*, 18702−18712.

(57) Chen, Y. Z.; Wang, C. M.; Wu, Z. Y.; Xiong, Y. J.; Xu, Q.; Yu, S. H.; Jiang, H. L. From bimetallic metal-organic framework to porous carbon: High surface area and multicomponent active dopants for excellent electrocatalysis. *Adv. Mater.* **2015**, *27*, 5010−5016.

(58) Qian, Y. H.; An, T.; Birgersson, K. E.; Liu, Z. L.; Zhao, D. Web-like interconnected carbon networks from NaCl-assisted pyrolysis of

ZIF-8 for highly efficient oxygen reduction catalysis. *Small* **2018**, *14*, No. 1704169.

(59) Wang, J.; Chen, Y. S.; Zhang, S. S.; Yang, C.; Zhang, J. Y.; Su, Y. Q.; Zheng, G.; Fang, X. S. Controllable states and porosity of Cu-carbon for CO_2 electroreduction to hydrocarbons. *Small* **2022**, *18*, No. 2202238.

(60) Midgley, P. A.; Weyland, M. 3D electron microscopy in the physical sciences: The development of Z-contrast and EFTEM tomography. *Ultramicroscopy* **2003**, *96*, 413−431.

(61) Ji, S. F.; Chen, Y. J.; Wang, X. L.; Zhang, Z. D.; Wang, D. S.; Li, Y. D. Chemical synthesis of single atomic site catalysts. *Chem. Rev.* **2020**, *120*, 11900−11955.

(62) Wang, C.; Kuai, L.; Cao, W.; Singh, H.; Zakharov, A.; Niu, Y. R.; Sun, H. X.; Geng, B. Y. Highly dispersed Cu atoms in MOF-derived N-doped porous carbon inducing Pt loads for superior oxygen reduction and hydrogen evolution. *Chem. Eng. J.* **2021**, *426*, No. 130749.

(63) Lai, B. L.; Wei, H. X.; Luo, Z. N.; Zheng, T.; Lin, Y. H.; Liu, Z. Q.; Li, N. ZIF-8-derived Cu, N co-doped carbon as a bifunctional cathode catalyst for enhanced performance of microbial fuel cell. *Sci. Total Environ.* **2023**, *856*, No. 159083.

(64) Zhu, W. J.; Ndayiragije, S.; Zuo, X. H.; Zhang, X. F.; Wang, G. H.; Wang, X. B. ZIF-8-derived single-atom Cu and N co-coordinated porous carbon as bifunctional material for SMX removal. *J. Environ. Chem. Eng.* **2022**, *10*, No. 107758.

(65) Sun, T. T.; Li, Y. L.; Cui, T. T.; Xu, L. B.; Wang, Y. G.; Chen, W. X.; Zhang, P. P.; Zheng, T. Y.; Fu, X. Z.; Zhang, S. L.; Zhang, Z. D.; Wang, D. S.; Li, Y. D. Engineering of coordination environment and multiscale structure in single-site copper catalyst for superior electrocatalytic oxygen reduction. *Nano Lett.* **2020**, *20*, 6206−6214.

(66) Liu, H. L.; Chang, Z. L.; Fu, J.; Hou, Z. Y. A CuZn-BTC derived stable $Cu/ZnO@SiO_2$ catalyst for ethanol dehydrogenation. *Appl. Catal., B* **2023**, *324*, No. 122194.

(67) Jin, W.; Lu, Z.; Wang, Q.; Zhu, Y.; Pan, H.; Yao, S.; Fang, Z.; Huang, X.; Chen, X. Atomic Cu dispersed ZIF-8 derived N-doped carbon for high-performance oxygen electrocatalysis in Zn-air battery. *J. Phys.: Mater.* **2021**, *4*, No. 024006.

(68) Zhang, L. Y.; Li, Y. Y.; Zhang, L.; Wang, K.; Li, Y. B.; Wang, L.; Zhang, X. Y.; Yang, F.; Zheng, Z. P. Direct visualization of the evolution of a single-atomic cobalt catalyst from melting nanoparticles with carbon dissolution. *Adv. Sci.* **2022**, *9*, No. 2200592.

(69) Huang, K. M.; Chen, S. Y.; Xia, C. J.; Li, C. H.; Zhu, B.; Gao, H. Y.; Peng, X. X.; Lin, M.; Luo, Y. B.; Wang, G.; Shu, X. T. HKUST-1 derived $Cu@CuO_x$/carbon catalyst for base-free aerobic oxidative coupling of benzophenone imine: High catalytic efficiency and excellent regeneration performance. *RSC Adv.* **2020**, *10*, 36111−36118.

(70) Tomson, N. C.; Williams, K. D.; Dai, X.; Sproules, S.; DeBeer, S.; Warren, T. H.; Wieghardt, K. Re-evaluating the Cu K pre-edge XAS transition in complexes with covalent metal−ligand interactions. *Chem. Sci.* **2015**, *6*, 2474−2487.

(71) Gougoussis, C.; Rueff, J.-P.; Calandra, M.; d'Astuto, M.; Jarrige, I.; Ishii, H.; Shukla, A.; Yamada, I.; Azuma, M.; Takano, M. Multiple pre-edge structures in Cu *K*-edge x-ray absorption spectra of high-T_c cuprates revealed by high-resolution x-ray absorption spectroscopy. *Phys. Rev. B* **2010**, *81*, No. 224519.

(72) Zhao, X.; Fang, R. Q.; Wang, F. L.; Kong, X. P.; Li, Y. W. Atomic design of dual-metal hetero-single-atoms for high-efficiency synthesis of natural flavones. *Nat. Commun.* **2022**, *13*, No. 7873.

(73) Gaur, A.; Shrivastava, B. D.; Joshi, S. K. Copper K-edge XANES of Cu(I) and Cu(II) oxide mixtures. *J. Phys.: Conf. Ser.* **2009**, *190*, No. 012084.

(74) Guda, A. A.; Guda, S. A.; Martini, A.; Kravtsova, A. N.; Algasov, A.; Bugaev, A.; Kubrin, S. P.; Guda, L. V.; Šot, P.; van Bokhoven, J. A.; Copéret, C.; Soldatov, A. V. Understanding X-ray absorption spectra by means of descriptors and machine learning algorithms. *NPJ Comput. Mater.* **2021**, *7*, No. 203.

(75) Shimizu, K. I.; Maeshima, H.; Yoshida, H.; Satsuma, A.; Hattori, T. Ligand field effect on the chemical shift in XANES spectra of Cu(II) compounds. *Phys. Chem. Chem. Phys.* **2001**, *3*, 862−866.

(76) Ren, X. J.; Quan, Y.; Yang, W.; Zhao, J. X.; Shi, R. N.; Ren, J. Highly efficient super activated carbon supported ultra-low loading copper catalyst for the oxidative carbonylation of methanol to dimethyl carbonate. *Mol. Catal.* **2022**, *531*, No. 112694.

(77) Sun, C. M.; Meng, F. H.; Wang, J. J.; Li, Z. CoZn-ZIF-derived carbon-supported Cu catalyst for methanol oxidative carbonylation to dimethyl carbonate. *New J. Chem.* **2022**, *46*, 7452−7463.

(78) Frank, P.; Benfatto, M. Symmetry breaking in solution-phase $[Cu(tsc)_2(H_2O)_2]^{2+}$: emergent asymmetry in Cu-S distances and in covalence. *J. Phys. Chem. B* **2021**, *125*, 10779−10795.

(79) Frank, P.; Benfatto, M.; Hedman, B.; Hodgson, K. O. The x-ray absorption spectroscopic model of the copper(II) imidazole complex ion in liquid aqueous solution: a strongly solvated square pyramid. *Inorg. Chem.* **2012**, *51*, 2086−2096.